Open-system ^{182}W–^{142}Nd isotope evolution of the early Earth

Seema Kumari[1,2], Andreas Stracke[2*], Debajyoti Paul[1]

[1] *Department of Earth Sciences, Indian Institute of Technology Kanpur, Kanpur 208016, Uttar Pradesh, India*

[2] *Westfälische Wilhelms Universität, Institut für Mineralogie, Corrensstr. 24, 48149 Münster, Germany.*

*Corresponding author

Email: astra_01@uni-muenster.de (Andreas Stracke)

Abstract

We present a five-reservoir open-system model for the ^{182}Hf–^{182}W and ^{146}Sm–^{142}Nd isotope evolution of the Earth to constrain early mantle-crust exchange and late accretion processes. In the presented model, core formation is complete within 30–100 Myr after solar system formation. The complementary bulk silicate Earth (BSE) differentiates to form a continental crust (CC), an incompatible element depleted upper mantle (UM), an initially primitive but continuously evolving lower mantle (LM), and an isolated reservoir (IR) where the recycled crust is stored for 1 Gyr before mixing into the LM. Late accretion adds bulk Earth-like material to the mantle after core formation, concurrent to progressive silicate differentiation. The ^{182}W and ^{142}Nd isotope evolution in each reservoir is calculated with a series of differential equations that compute the changing abundance of each isotope from the start of solar system evolution (t = 4.56 Ga) to the present (t = 0 Ga). Core formation until at least 45–60 Myr after solar system initial is most compatible with the modeled ^{182}W evolution of the silicate Earth, which limits the amount of late accreted material to about 1.0–0.5%. However, the pre-late accretion μ^{182}W and Hf/W (or W) of the BSE depend strongly on the rate and duration of core formation and determine the amount of late accreted material necessary to evolve to the present $\mu^{182}W_{BSE} \sim 0$. The interdependency of these parameters is key for evaluating the variable influence of late accretion and early mantle-crust interaction on the Hf-W evolution of the BSE. Nevertheless, heterogeneous distribution of the late accreted material to the mantle, in combination with Hadean crust formation and recycling is required to form a mantle reservoir with a small range of ^{182}W excesses between 10–15 ppm throughout the Archean, as observed in most Archean rocks. Reproducing the observed ^{142}Nd and ^{182}W signatures in Hadean-Eoarchean mantle-derived rocks with our model further requires that continental crust starts to form within the first ∼50 Myr after core formation. Continuous exchange between the crust and the different mantle reservoirs in our model leads to post-Archean homogenization of early-formed ^{182}W and ^{142}Nd heterogeneities and development of present bulk silicate earth values in all silicate reservoirs. But if part of the recycled CC in our model is isolated from further exchange with other crustal and mantle reservoirs, the average LM reservoir in the presented model maintains slightly negative μ^{182}W since late accretion, which provides a possible explanation for the observed ^{182}W deficits in some young ocean island lavas.

Keywords: Hf-W isotope system, ^{142}Nd, open system evolution, late accretion, core formation, early earth

1. INTRODUCTION

Owing to the limited rock record of Hadean and Archean rocks, our understanding of the geodynamic processes during Earth's earliest evolutionary phase remains rudimentary. The ^{182}Hf–^{182}W systematics of meteoritic and planetary samples have shown that terrestrial core formation occurred within the first 30–100 Myr of solar system formation (e.g., Lee and Halliday, 1995; Harper and Jacobsen, 1996; Kleine et al., 2002; 2009; Yin et al., 2002; Halliday and Wood, 2009). Continued accretion after core formation added further material, which determined the mantle abundances of the highly siderophile elements (HSE: Re, Os, Ir, Ru, Pt, Rh, Pd, and Au) and influenced Earth's ^{182}W isotope evolution (Kimura et al., 1974; Kleine, 2011). It remains debated when core formation ceased, and thus when late accretion began, how long the late accretion phase lasted, and if dispersal of late-accreted material created transient, but variably long-lived HSE and ^{182}W isotope heterogeneities in the Earth's mantle. Van de Löcht et al. (2018), for example, argued that mantle rocks younger than 3.8 Ga have HSE abundances similar to the modern mantle, suggesting termination of late accretion and complete homogenization of the accreted material at ~3.8 Ga. Others argue for longer homogenization timescales based on lower than present HSE abundances in komatiites older than ~3.0 Ga (Maier et al., 2009). Concurrent to late accretion, Earth's earliest crust started to form (e.g., Wilde et al., 2001; Harrison et al., 2008), which initiated the progressive compositional differentiation of the silicate Earth.

The short-lived radioactive decay systems ^{182}Hf–^{182}W ($t_{1/2}$ = 8.9 Myr) and ^{146}Sm–^{142}Nd ($t_{1/2}$ = 103 Myr) are variably sensitive to the different geodynamic processes during Earth's earliest evolutionary phase (e.g., Kleine et al., 2002; Boyet and Carlson, 2005; Caro, 2011; Kleine, 2011; Kleine and Walker, 2017; Rizo et al., 2016; Rosas and Korenaga, 2018; Carlson et al., 2019). Owing to the moderately siderophile behavior of W under highly reducing conditions, the ^{182}Hf–^{182}W decay system is mostly sensitive to metal–silicate fractionation during core formation or early magma ocean crystallization (e.g., Kleine et al., 2009). However, under more oxidizing conditions typical of silicate differentiation processes after core formation, W is lithophile and more incompatible than Hf (Newsom et al., 1996; Righter and Shearer, 2003; Arevalo and McDonough, 2008). Early crust formation and concurrent mantle depletion therefore also influence the ^{182}W evolution of the silicate Earth, if they start within the lifetime of ^{182}Hf. On the other hand, because Sm and Nd are refractory lithophile elements (Nd is more incompatible than Sm), the ^{146}Sm–^{142}Nd decay system is controlled exclusively by the timing and nature of silicate differentiation within the first ~500 Myr of Earth's history (e.g., Jacobsen and Harper, 1996; Boyet and Carlson, 2005, Caro et al., 2006; Roth et al., 2013).

Most mantle-derived rocks older than 2.4 Ga have non-zero μ^{182}W within a narrow range of about +10 to +15 (μ^{182}W is the ppm deviation in ^{182}W/^{184}W relative to the present terrestrial standard), which are variably attributed to core formation, non-uniform distribution of late accreted material within the mantle, and silicate melt-crystal or metal-silicate fractionation in an early magma ocean (e.g., Willbold et al., 2011; Touboul et al., 2012; Touboul et al., 2014; Liu et al., 2016; Puchtel et al., 2016; Puchtel et al., 2018; Archer et al., 2019; Tusch et al., 2019). Despite μ^{182}W within a narrow range of +10 to +15, μ^{142}Nd in Archean mantle-derived

rocks vary from positive to negative values (μ^{142}Nd is the ppm deviation in ^{142}Nd/^{144}Nd relative to the present terrestrial standard), indicating that chemically distinct crustal and mantle reservoirs started to form within the first ~500 Myr of Earth's history (e.g., Bennett et al., 2007; Rizo et al., 2011; O'Neil et al., 2016). The 3.8–3.3 Ga old rocks from the Isua Supracrustal Belt, Greenland, for example, have μ^{182}W >0 and μ^{142}Nd >0 (Willbold et al., 2011; Rizo et al., 2016). On the other hand, ~3.5–3.3 Ga old rocks from the Pilbara Craton, Western Australia, have μ^{182}W >0 but μ^{142}Nd ~0 (Archer et al., 2019), and the ~4.0–3.6 Ga old rocks from the Acasta Gneiss Complex, Canada have μ^{182}W >0 and μ^{142}Nd <0 (e.g., Roth et al., 2014; Willbold et al., 2015; Reimink et al., 2018). With μ^{182}W <0 and μ^{142}Nd <0, the ~3.5 Ga old Schapenburg komatiites are an exception (Puchtel et al., 2016). Variable ^{142}Nd excesses and deficits coupled with excess ^{182}W of similar magnitude in most Archean mantle-derived rocks imply that heterogeneous early-formed mantle and crustal components are part of their mantle source(s). In contrast, post-Archean rocks are generally similar to the modern accessible mantle with μ^{182}W ~0 and μ^{142}Nd ~0 (Rizo et al., 2013; Mundl et al., 2018; Rizo et al., 2019), indicating progressive homogenization of Hadean and early Archean ^{182}W and ^{142}Nd heterogeneities. However, some young ocean island basalts (OIB) have μ^{182}W <0, which require either the preservation of ^{182}W deficits produced during the life-time of ^{182}Hf or incorporation of core material with μ^{182}W ~ –200 (Mundl et al., 2017; Mundl-Petermeier et al., 2020; Rizo et al., 2019).

Here, we present an open system model for the isotopic evolution of Earth's major reservoirs, which is adapted from the model presented by Kumari et al. (2016, 2019) by incorporating the ^{146}Sm–^{142}Nd and ^{182}Hf–^{182}W isotope systematics, and by implementing an additional core reservoir within a five-reservoir model of Earth's isotopic evolution. The model quantitatively evaluates how (i) the duration and rate of core formation influence the pre-late accretion μ^{182}W, W concentration and Hf/W ratio of the bulk silicate earth and how the interdependency with (ii) the amount, rate, and style of late accretion, and (iii) the timing and nature of silicate differentiation (i.e., crust formation and crust-mantle interaction) affects the ^{182}W and ^{142}Nd isotope evolution of the evolving silicate Earth.

2. METHODS: OPEN SYSTEM EVOLUTION OF THE EARTH

2.1. General model set-up

The model presented here is an extended version of the model presented by Kumari et al. (2016, 2019), which uses the long-lived U–Th–Pb, Rb–Sr, Sm–Nd, and Lu–Hf isotope systematics to quantify mass fluxes between a bulk continental crustal reservoir (CC), and two different mantle reservoirs to simulate the geochemical evolution of the silicate Earth. The modeled mantle reservoirs consist of an incompatible element depleted, so-called upper mantle (UM), and a non-primitive lower mantle (LM). In addition, there is an isolated reservoir (IR), where recycled continental crust is stored before being transferred into the LM. In this open system, or "box modeling" approach, radiogenic isotope ratios in a reservoir are functions of the parent-daughter ratios in each reservoir as well as the fluxes into and out of the reservoirs (e.g., Paul et al., 2002; Kumari et al., 2016).

Here, we extend the open system model of Kumari et al. (2016, 2019) by including an additional core reservoir. Starting with the elemental inventory of bulk earth, the core forms in different time periods, by mass and species (i.e., the moderately siderophile element W) exchange between core and mantle until the core has reached its present mass (see Fig. 1, section 2.3 and the supplementary material for equations describing the rate of mass and species exchange between core and mantle). Core formation results in formation of a complementary silicate reservoir, the bulk silicate earth (BSE), with initial μ^{182}W, W concentration and Hf/W determined by the duration and rate of core formation (section 2.3). After core formation, late accretion of bulk Earth-like material and concurrent silicate differentiation into bulk crust and different mantle reservoirs regulate the ^{182}Hf–^{182}W and ^{146}Sm–^{142}Nd isotope evolution in this five-reservoir model of Earth's isotopic evolution.

Specifically, the CC grows by mass fluxes from the LM and UM reservoirs and shrinks by recycling into the mantle (Fig. 1). One fraction of the recycled crustal material goes into the UM, which can be varied with the model parameter f_R (f_R has a default value of 0.4, Kumari et al., 2016). The remainder, $1-f_R$, is stored in the IR before being transferred to the LM. The default storage time in the IR is 1 Gyr, but shorter and longer residence times are also explored. Long residence times (>4.5 Ga), for example, simulate formation of an early reservoir that remains isolated for the rest of Earth's history (e.g., Boyet and Carlson, 2005). The outgoing flux into the CC and the influxes from the CC, LM, and late accreted material determine the evolution of the UM (Fig. 1). The LM evolves by the initial influx from late accreted material, and the continuous influx of recycled CC after transient storage in the IR, and the outgoing fluxes into the UM and CC (Fig. 1).

A series of first-order differential equations, describing the changing abundance of each isotope species in each reservoir, is solved numerically using the fourth-order Runge-Kutta method at 1 Myr time steps from 4.56 Ga to the present (see supplementary material of Kumari et al., 2016 for details and also supplementary material of this study for additional equations constraining the core-mantle mass and species exchange). The set of fixed and variable model parameters (Tables S1-S3) are discussed in detail in Kumari et al. (2016, 2019). These include reservoir masses (M), the residence or isolation time (IT) of the recycled CC material in the IR, and bulk mass or elemental transfer factors (D_i) between the different reservoirs, which are constrained by simultaneously reproducing the estimated present-day average elemental abundances and isotope ratios of each reservoir (Tables 1-3). These present terrestrial reservoir compositions are constrained by global data of mid-ocean ridge basalts (MORB, UM), plume-derived ocean island basalts (OIB, LM), and the continental crust (CC) (see details in Kumari et al., 2016, 2019). The composition of the additional core reservoir in the model presented here (Table 2) is taken from estimates of Arevalo and McDonough (2008) and McDonough (2014).

Note that the mass transfer factor D_i in our model is *NOT* a bulk solid-melt partition coefficient, but rather a parameter that represents the combined mass transfer for each element i between the different reservoirs (Paul et al., 2002). Mass transfer could result from several processes such as one or more melting events, potential fluid transport, etc. A value of D_i >1 enriches, and a value of D_i <1 depletes a given reservoir in the element i. Based on constraints

from the long-lived radioactive decay systems (Rb-Sr, Sm-Nd, Lu-Hf, U-Pb, Kumari et al., 2016 and 2019), our model assumes exponential crustal growth with 90% of the flux coming from the UM and the remainder from the LM, resulting in a present mass fraction of the UM reservoir ($m_{UM} = M_{UM}/M_M$) of ~0.5–0.6. Because the majority of the CC is thus formed from the UM, the model parameter m_{UM} effectively controls the concentration of each element in the UM ($C^i_{UM} = M^i_{UM}/(M_M \times m_{UM})$; where C^i_{UM} is the concentration of element i in the UM, M^i_{UM} is the mass of element i in the UM, and M_M is the total mantle mass). We have also performed model simulations by varying the parameters m_{UM}, f_R, D_i, and the residence time of recycled crust in the IR to explore different scenarios that satisfy the observational constraints from the ^{182}W and ^{142}Nd data in Archean rocks.

2.2. Initial state of the model

The initial bulk Earth abundances of ^{146}Sm, ^{182}Hf, and ^{182}W were calculated using the solar system initial isotope ratios of $^{146}Sm/^{144}Sm = 0.0085$ (Boyet et al., 2010), $^{182}Hf/^{180}Hf = 1.018\times10^{-4}$ (Burkhardt et al., 2008), and $^{182}W/^{184}W = 0.864598$ (Kleine and Walker, 2017), and the present abundances of the stable isotopes ^{144}Sm, ^{180}Hf, and ^{184}W. The abundances of the stable isotopes (^{144}Sm, ^{180}Hf, ^{184}W) are calculated using their present relative abundances and concentrations of Sm, Hf, and W in the bulk Earth (Table 1). The solar system initial $^{142}Nd/^{144}Nd_i$ is calculated using the following equation:

$$^{142}Nd/^{144}Nd_t = {}^{142}Nd/^{144}Nd_i + (^{146}Sm/^{144}Sm)_I\,(^{144}Sm/^{147}Sm)_P\,(^{147}Sm/^{144}Nd)_P\,(1-e^{-\lambda 146\times t}) \quad (1)$$

where t is the time from the origin of the solar system to the present. Further, the $(^{147}Sm/^{144}Nd)_p$ and $(^{144}Sm/^{147}Sm)_p$ are calculated using the present abundances of isotopes and concentrations of Sm and Nd in the bulk Earth (Table 1). The calculated initial abundances of all modeled radioactive parents, radiogenic daughters, and stable isotopes in the bulk Earth are given in the supplementary material (Table S4).

2.3. Core formation

In our model, core formation begins at t = 4.56 Ga (the start of solar system condensation) and starts with the mass (5.94×10^{24} kg) and elementary inventory (Sm, Nd, Hf, W) of the bulk Earth (Table 1). In the default model set-up, the core grows linearly to its present mass of 1.883 $\times 10^{24}$ kg for periods of 30, 45, 60, or 100 Myr. The 30 Myr core formation period is one end-member case, constrained by single-stage instantaneous ^{182}Hf–^{182}W core growth models (Kleine et al., 2009). For the 100 Myr end-member, ^{182}Hf is almost completely extinct at the end of core formation.

In each increment of core formation, W goes into the core, but Hf, Sm, and Nd stay in the complementary silicate reservoir, the bulk silicate earth (BSE). The BSE thus maintains chondritic Sm/Nd and $\mu^{142}Nd$ values until the end of core formation, but evolves to progressively lower W concentrations (W_{BSE}) and higher Hf/W_{BSE} and $\mu^{182}W_{BSE}$ values. The latter are determined by the rate and overall magnitude of the W flux to the core, which in our model, is controlled by the bulk silicate-metal transfer factor, $D_{W,silicate\text{-}metal}$. The Hf/W_{BSE} (W_{BSE}) and $\mu^{182}W_{BSE}$ values at the end of core formation define the subsequent ^{182}W evolution

of the BSE, but unfortunately remain unknown (Kruijer et al., 2015, Touboul et al., 2015). We therefore use the present $\mu^{182}W_{BSE}$ to constrain the ^{182}W evolution of the BSE. The present $\mu^{182}W_{BSE}$ is 0 by definition, but has been lowered by continued accretion after core formation, during the so-called 'late accretion' phase. Recent estimates of the present, pre-late-accretion $\mu^{182}W_{BSE}$ range from +10 and +40 (Kruijer et al., 2015; Touboul et al., 2015). We use a $\mu^{182}W_{BSE}$ target value in the middle of this estimated range, and adjust $D_{W,silicate\text{-}metal}$ for each given core formation period such that the BSE evolves to $\mu^{182}W$ = +25 at the present day, without adding any late accreted material.

This strategy allows exploring how different rates of core formation, simulated by varying $D_{W,silicate\text{-}metal}$, influence the modeled W_{BSE}, Hf/W_{BSE}, and $\mu^{182}W_{BSE}$ values at the end of core formation, and how these different starting values change the ^{182}W evolution of the evolving crust and mantle reservoirs during subsequent late accretion and silicate differentiation processes (see detailed discussion in sections 3.1, 4.1).

An alternative strategy would be to assume that the present pre-late accretion $\mu^{182}W_{BSE}$ value (+25) is equivalent to the $\mu^{182}W_{BSE}$ value at the end of core formation. But this assumption inherently implies that there is no contribution of radiogenic ^{182}W to the ^{182}W budget of the BSE after core formation ended, that is, late accretion started after ^{182}Hf became extinct (>80-100 Myr). Although this may be a viable assumption (e.g., Maurice et al., 2020), the duration of core formation remains unknown (e.g., Rudge et al., 2010). Moreover, despite the short ca. 8.9 Myr half-life of ^{182}Hf, radiogenic ^{182}W contributes significantly to the ^{182}W budget of the BSE, if core formation is shorter than ~80 Myr (Fig. 2). Hence to allow for different core formation periods, and thus starting times of late accretion, we used the core growth model described above, and discussed in more detail in section 3.1, to constrain the $\mu^{182}W_{BSE}$ and Hf/W_{BSE} (W_{BSE}) at the end of core formation.

Any deviations from the default linear core formation model, for example a large mass and thus W flux to the core early or late during core formation (e.g., by a giant impact), influence the initial $\mu^{182}W_{BSE}$, W_{BSE} and Hf/W_{BSE} at the start of late accretion, and thus the subsequent ^{182}W evolution of all silicate reservoirs (Fig. 3). Different, non-linear core formation scenarios are therefore also explored, and discussed in more detail in sections 3.1 and 4.1.

In addition, the comparatively large uncertainty of the present, pre-late accretion $\mu^{182}W_{BSE}$ target value, with a possible range of values between +10 and +40, affects the modeled $\mu^{182}W_{BSE}$ evolution. This uncertainty is caused by the large uncertainty of the parameters required to make this estimate (Kruijer et al., 2015; Touboul et al., 2015). Namely, the amount and type of late accreted material, which is derived from the HSE concentrations of the BSE, but especially the W_{BSE} (13 ± 10 ppb, 2SD, Arevalo and McDonough, 2008). The chosen target value in our model, $\mu^{182}W_{BSE}$ = +25, is therefore by no means a robust constraint. How these imposed uncertainties on the $\mu^{182}W_{BSE}$ evolution influence other model-derived constraints, e.g., the mass of late accreted material, is discussed in detail in sections 3.2 and 4.2.

2.4. Late accretion

Late accretion is the addition of extra-terrestrial material to Earth after the end of core formation (Chou, 1978; Walker, 2009). In our model, late accretion thus starts with the end of

core formation at 30, 45, 60 or 100 Myr after solar system formation (4.56 Ga) and ends at 3.8 Ga. Addition of late accreted material until 3.8 Ga marks the end of the so-called 'lunar cataclysm' (Tera et al., 1974), which is often considered as the end of the late accretion period (e.g., Maier et al., 2009; van de Löcht et al., 2018). The late accreted material (also termed 'late veneer') used in this study has Hf and W abundances similar to estimates for bulk Earth (C_W = 180 ppb, C_{Hf} = 197 ppb; Table 1; McDonough, 2014) and a μ^{182}W of –190 ± 10 (Kleine et al. 2004). The late accreted material (LAM) is added until the BSE has a μ^{182}W ~ 0 at 3.8 Ga similar to its present value. The target for the evolution of the UM reservoir is the narrow range of μ^{182}W values between +10 and +15 that is observed in most mantle-derived Archean rocks (4.0–2.5 Ga), and the μ^{182}W ~0 for post-Archean basalts (e.g., Mundl et al., 2018; Rizo et al., 2019).

We investigate different styles of late accretion. During uniform, or homogeneous late accretion, the fraction of LAM going to the UM and LM is proportional to the mass of these mantle reservoirs (section 3.4.1). Non-uniform or heterogeneous late accretion is when the UM reservoir receives a smaller relative fraction of the incoming material than the LM reservoir (section 3.4.2). Note that although we use the terminology of upper and lower mantle (UM and LM), there is no spatial connotation implied. Rather, these two boxes in our model should simply be perceived as two different mantle reservoirs that can receive different amounts of LAM (and have different in-and outgoing fluxes from and to the crust).

We also simulate different rates of late accretion, for example adding a significant fraction of the material at the beginning or end of the late accretion period, which simulates sudden addition of large single bodies versus addition of a fixed amount per time interval (linear flux rate). How the different rates, but also composition of the late accreted materials (e.g., differentiated vs. undifferentiated objects) affect the μ^{182}W evolution of the different silicate reservoirs, as well as the geodynamic implications of the different late accretion scenarios will be discussed in detail in sections 3.3 and 4.2.

3. RESULTS

3.1. Effect of core formation on the pre-late accretion W_{BSE}, Hf/W_{BSE}, and $\mu^{182}W_{BSE}$

The evolution of $\mu^{182}W_{BSE}$ for core formation periods of 30, 45, 60 and 100 Myr is shown in Fig. 4. In each case, $\mu^{182}W_{BSE}$ evolves to the chosen present target value of +25 without late accretion (Kruijer et al., 2015; Touboul et al. 2015; Kruijer and Kleine, 2017).

Notably, even for a core formation period of 60 Myr, when ^{182}Hf is nearly extinct, a minute amount ^{182}Hf is left over in the BSE ($^{182}Hf/^{180}Hf_{BSE}$ >0, Fig. 2), which leads to a subsequent increase of $\mu^{182}W_{BSE}$, if not counteracted by the addition of late accreted material (Fig. 4). Hence, for core formation times, t_{CF}, less than ~80 Myr (Figs. 2 and 4), the duration of core formation influences $\mu^{182}W_{BSE}$ considerably and, depending on Hf/W_{BSE} at t_{CF}, determines how much radiogenic ^{182}W is produced in the BSE after core formation.

Different $\mu^{182}W_{BSE}$ and Hf/W_{BSE} ($^{180}Hf/^{184}W_{BSE\ t=0}$) at t_{CF} for different rates and durations of core formation (Figs. 3 and 4) result from different mass and associated W flux rates required to accumulate the total mass of the core over different core formation periods. The W flux rate to the core is controlled by the silicate-metal transfer factor $D_{W,silicate\text{-}metal}$ in our model (section

2.3). Different $D_{W,silicate\text{-}metal}$ values lead to different W_{BSE} and W_{core} at t_{CF} (Table 4). Because Hf remains entirely in the evolving BSE, the different Hf/W_{BSE} at t_{CF} thus result solely from the different W_{BSE} values at t_{CF}. Hence the $D_{W,silicate\text{-}metal}$ is set such that the Hf/W_{BSE} and $\mu^{182}W_{BSE}$ at t_{CF} lead to the present pre-late accretion target value $\mu^{182}W_{BSE}$ of +25 (Table 4; Fig. 4, eqn 2), which is calculated by:

$$^{182}W/^{184}W_{BSE\ t=0} = {}^{182}W/^{184}W_{BSE,tCF} + [{}^{182}Hf/^{180}Hf_{tCF} \times {}^{180}Hf/^{184}W_{BSE,t=0}] \quad (2)$$

For our default linear core formation model, the $\mu^{182}W_{BSE}$ at t_{CF} ($^{182}W/^{184}W_{BSE\ tCF}$) decreases for shorter core formation periods, t_{CF} (Table 4; Fig. 4). But because $^{182}Hf/^{180}Hf_{tCF}$ increases exponentially with shorter t_{CF} during the lifetime of ^{182}Hf, Hf/W_{BSE} ($^{180}Hf/^{184}W_{BSE,t=0}$) also has to decrease to evolve to a fixed present $\mu^{182}W_{BSE}$ ($^{182}W/^{184}W_{BSE,t=0}$, Table 4). Shorter core formation periods during the lifetime of ^{182}Hf therefore lead to lower $\mu^{182}W_{BSE}$, but also require lower Hf/W_{BSE} at t_{CF} to evolve to the same present pre-late accretion $\mu^{182}W_{BSE}$ of +25 (Table 4; Figs. 3 and 4). The low Hf/W_{BSE} values at t_{CF} for short core formation times are due to high W_{BSE} values caused by low $D_{W,silicate\text{-}metal}$ values (Table 4).

Any deviations from the default linear core formation model, for example a large mass and thus W flux to the core early or late during a given core formation period, influence the $\mu^{182}W_{BSE}$, Hf/W_{BSE} (W_{BSE}) values at the end of core formation, t_{CF} (Table 4; Fig. 3). For fast core growth rates early during a given core formation period, $\mu^{182}W_{BSE}$ at t_{CF} increases compared to the linear core growth model (Table 4; Fig. 3). As the value of $(^{182}Hf/^{180}Hf)_{tCF}$ is only a function of t_{CF}, higher $\mu^{182}W_{BSE}$ at t_{CF} in response to fast early core growth rates during a given core formation period therefore require lower Hf/W_{BSE} to get the same present $\mu^{182}W_{BSE}$ (+25, Fig. 3).

Hence, different rates and durations of core formation cause variable $\mu^{182}W_{BSE}$, Hf/W_{BSE}, and W_{BSE} at the end of core formation or start of the late accretion period (Figs. 3 and 4). Ultimately, these different BSE starting values determine the subsequent ^{182}W isotope evolution of the BSE, and influence other model-derived constraints, foremost the amount of late accreted material required to evolve to $\mu^{182}W_{BSE} = 0$ at the end of the late accretion period, as discussed in the following.

3.2 The relation between the rates of core growth and the amount of late accretion

The amount of late accreted material (LAM) and the rate and duration of core formation are interdependent parameters, because the different $\mu^{182}W_{BSE}$ and Hf/W_{BSE} (W_{BSE}) values in response to different rates and durations of core growth determine how much LAM is required to evolve to $\mu^{182}W_{BSE} = 0$ at the end of the late accretion period (3.8 Ga). In our default linear core growth model, the amount of LAM varies from 1.9% to 0.07% relative to the bulk Earth mass for core formation periods between 30 and 100 Myr, and is largest for short core formation periods (Table 4; Fig. 4). Longer core formation periods require less LAM, mainly because W_{BSE} at t_{CF} is lower, and although Hf/W_{BSE} and $\mu^{182}W_{BSE}$ are higher compared to shorter core formation periods (Table 4; Fig. 4; section 3.1).

Any deviations from the linear core formation model, for example rapid early or late core growth, and thereby a large W flux to the core early or late in the pre-late accretion period (e.g., following the moon-forming impact), considerably influence the $\mu^{182}W_{BSE}$ and W_{BSE} (or

Hf/W_{BSE}) at the start of the late accretion period, and thus also the amount of LAM required to evolve to $\mu^{182}W_{BSE}$ ~0 at the end of late accretion (Fig. 3 shows results for t_{CF} = 45 Myr, Table 4). Rapid early core growth leads to higher $\mu^{182}W_{BSE}$ and $^{182}W_{BSE}$ (lower Hf/W_{BSE}) immediately after core formation and require a larger mass of LAM compared to linear core growth (Fig. 3; Table 4). A rapid rate of core growth late during the core formation period, for example by a giant impact, leads to lower $\mu^{182}W_{BSE}$ and W_{BSE} (higher Hf/W_{BSE}) immediately after core formation and requires a smaller mass of LAM compared to linear core growth (Fig. 3; Table 4). The rate and duration of core formation thus have a large influence on the $\mu^{182}W$ and W concentration (Hf/W) of the BSE and thus also the amount of LAM inferred from the ^{182}W systematics. Similar effects are also observed for other core formation periods of 30, 60, and 100 Myr (Figs. S1-S3; Table 4).

The amount of LAM is most sensitive to W_{BSE} at the end of core formation (Table 4; Fig. 5). This is because late accretion essentially compensates for the excess ^{182}W that leads to the assumed $\mu^{182}W_{BSE}$ = +25 without late accretion, compared to $\mu^{182}W_{BSE}$ = 0 including LAM. This small amount of excess ^{182}W depends on the values of $\mu^{182}W_{BSE}$, Hf/W_{BSE} (W_{BSE}) and $^{182}Hf/^{180}Hf$ at the end of core formation (eqn. 2), and is therefore set entirely by the pre-late accretion processes (core formation rate in our model, see detailed discussion in sections 3.1 and 4.2). Because the absolute amount of excess ^{182}W scales with W_{BSE}, the amount of late accreted material needed to develop to $\mu^{182}W_{BSE}$ = 0 is most sensitive to W_{BSE} at t_{CF}. The lower W_{BSE} at t_{CF}, the smaller is the absolute amount of excess ^{182}W, and the smaller is the amount LAM required to develop to $\mu^{182}W_{BSE}$ = 0 at the end of late accretion (Table 4; Fig. 3).

Other than W_{BSE}, the composition of the LAM has an effect on the required amount of LAM. But since variable rates and duration of core formation result in highly variable W_{BSE} (Table 4), and if the variation in $\mu^{182}W$ of possible late accreted materials is comparatively small (Kleine et al., 2009; see further discussion in section 4.2), the composition of the LAM has a subordinate effect on the amount of LAM compared to the value of W_{BSE}, which is set by core formation (and early accretion, see further discussion in section 4.2).

3.3 ^{182}W isotope evolution of the BSE: influence of variable rates of late accretion

The shape of the $\mu^{182}W_{BSE}$ evolution curve during the late accretion phase depends strongly on the amount of LAM per time interval, that is, the rate of late accretion. The constant composition and amount of LAM per time interval in our default model (linear late accretion rate, Fig. 6a-b and section 2.4) leads to a linear decrease of $\mu^{182}W_{BSE}$ shortly after the end of core formation until $\mu^{182}W_{BSE}$ = 0 at the end of late accretion at 3.8 Ga. In contrast, adding 90% of the total amount of LAM to the mantle in the initial 100 Myr of late accretion (rapid late accretion scenario) leads to a rapid decrease of $\mu^{182}W_{BSE}$ in this time interval (Fig. 6a-b). When 90% of the total amount of LAM is added in the last 100 Myr of late accretion time (delayed late accretion scenario) the BSE maintains high $\mu^{182}W_{BSE}$ values, depending on the initial $\mu^{182}W_{BSE}$, and Hf/W_{BSE} at the start of late accretion (i.e., the rate and duration of core formation, section 3.1). Thereafter, $\mu^{182}W_{BSE}$ rapidly drops to 0 during this final late accretion phase (Fig. 6b).

Note, however, that the BSE evolution shown in Fig. 6b and d is essentially a theoretical reservoir evolution, because mantle-crust differentiation starts concurrent to late accretion, and thus the BSE reservoir ceases to exist with the start of late accretion. The subsequent silicate Earth evolution is effectively captured by the evolving mantle and crust reservoirs (UM, LM, IR, CC) in our model. The ^{182}W evolution of the evolving mantle and crustal reservoirs is influenced by several parameters. These are how the LAM is distributed between the different mantle reservoirs (UM and LM), and how the distribution of W between the evolving mantle and crustal reservoirs affects the W concentrations (and Hf/W) and thus the proportion of W from the LAM to the amount of W in each reservoir. The latter essentially regulates how sensitive each reservoir reacts to the incoming late accretion flux. Starting with the simplest case of uniform distribution of the LAM to the UM and LM (homogeneous late accretion) in the following (section 3.4.1), it will be discussed how the variable distribution of the LAM between the UM and LM (heterogeneous late accretion, section 3.4.2), and variable rates of late accretion affect their ^{182}W evolution (section 3.4.3).

3.4 Crust-mantle ^{182}W isotope evolution

3.4.1 Homogeneous late accretion

Figure 7 shows model results for uniform or homogeneous addition of the LAM to both the evolving UM and LM reservoir until 3.8 Ga for core formation periods of 30, 45, 60, and 100 Myr, using the set of model parameters listed in Table S2. For transfer from mantle to crust, the default bulk elemental enrichment factor for W between mantle and crust (D_W), is set equal to that of Th and U (~200) as used by Kumari et al. (2016) based on the assumption that W is similarly incompatible during silicate differentiation as U and Th (Righter and Shearer, 2003; Arevalo and McDonough, 2008).

In Fig. 7, all silicate reservoirs initially develop μ^{182}W >0 due to decay of left-over ^{182}Hf, which then variably decreases due to the addition of LAM with μ^{182}W = –190. Notably, the LM is the largest silicate reservoir in our model, but the bulk of the CC is formed by the mass flux from the UM (section 2.1, Kumari et al., 2016, 2019). This means there is only a small outgoing flux from the LM to the CC. The return-flux of the CC goes into the UM and IR (Figs. 1 and 7). Because the isolation time of the recycled material in the IR is ~1 Gyr before mixing into the LM, there is effectively no incoming flux of recycled CC into the LM until 1 Gyr after core formation (~3.5 Ga). Even thereafter, the effect on $\mu^{182}W_{LM}$ is minimal owing to the small amount of W in the recycled crust relative to the large amount of W in the LM. Hence, the LM maintains a 'near-primitive' composition and thus evolves similarly to the BSE until the end of the late accretion period (3.8 Ga), and subsequently maintains a μ^{182}W ~0 (for all four core formation periods).

The CC is formed mostly by the mass flux from the UM (Fig. 1, section 2.1), and thus only little W is left in the UM leading to high Hf/W_{UM} values ($D_W > D_{Hf}$). Consequently, the UM is very sensitive to the addition of LAM, which changes its $\mu^{182}W_{UM}$ more easily than that of any other reservoir. In fact, the UM retains so little W after the core formation that the addition of small amounts of LAM overwhelm the otherwise increasing $\mu^{182}W_{UM}$ due its high Hf/W_{UM}, resulting in $\mu^{182}W_{UM}$ <0 in the Archean (Fig. 7).

There are two ways to counteract the evolving $\mu^{182}W_{UM}$ <0 in our model: (1) adding less LAM and (2) recycling crust (CC) with $\mu^{182}W_{UM}$ >0. Increasing the recycling flux of the CC into the UM relative to the IR by varying the parameter f_R (from 0.1 to 0.9, section 2.1) results in a less negative $\mu^{182}W_{UM}$ in the Archean (Fig. 7). But the effect is limited due to the relatively small mass of the CC at this time, and thus the small amount of W recycled into the UM. Therefore, the only way to counteract the negative $\mu^{182}W_{UM}$ is by non-uniform addition of LAM to the UM and LM, that is, by heterogeneous addition of the LAM to Earth's mantle.

3.4.2 Heterogeneous late accretion

Figure 8 shows the ^{182}W evolution in the different modeled silicate reservoirs when the LAM is added linearly, but non-uniformly, to both the UM and LM for a core formation period of 45 Myr, and late accretion until 3.8 Ga (model results for core formation periods of 30, 60 and 100 Myr are shown in Figures S4-S7). Adding only a small fraction (2%) of the total amount of LAM to the UM (and the remainder to the LM) leads to positive $\mu^{182}W_{UM}$ values at the beginning of the late accretion period (Figs. 8 and 9). Geodynamically, this corresponds to a scenario where parts of a progressively depleting mantle (the modeled UM) receive less LAM than other parts of the mantle (e.g., the LM in our model). The scenario where the UM receives only 2% of the total amount of LAM and the remaining 98% goes into the LM (Fig. 8) successfully reproduces the $\mu^{182}W_{UM}$ target range, i.e., the observed range of $\mu^{182}W$ ~ +10–15 of most Archean rocks.

The key parameters for achieving a successful solution shown in Fig. 8 are the non-uniform mixing of LAM into the mantle, and the recycling of CC with $\mu^{182}W$ >0. Addition of recycled crust with high $\mu^{182}W$ to the UM results in a significant increase in the $\mu^{182}W_{UM}$ in the Archean (Fig. 8). The kink in the $\mu^{182}W_{UM}$ evolution observed immediately after the end of late accretion at 3.8 Ga in Fig. 8 marks the effect of crustal recycling, which becomes more pronounced after the end of late accretion and protracts the time interval of $\mu^{182}W_{UM}$ ~+10–15 until the end of Archean. Hence, a balance between the addition of LAM with $\mu^{182}W$ <0 (–190) and recycling of CC with $\mu^{182}W$ >0 is essential for maintaining a near-constant $\mu^{182}W$ ~+10–15 in the UM over the entire duration of the Archean. Progressive interaction of crust and mantle afterwards slowly homogenizes $\mu^{182}W$ in the crust and mantle reservoirs resulting in a steady decrease of $\mu^{182}W$ in the CC and UM (and increase in LM) from ~+10–15 since the Archean towards the present $\mu^{182}W_{BSE}$ = 0.

However, maintaining $\mu^{182}W_{UM}$ in the range of +10 to +15 requires that the total amount of LAM added to the UM is comparatively small (2% of the total flux, Fig. 8). But even then, $\mu^{182}W_{UM}$ is between +10 and +15 only for a short time-period between 3.8 and 3.5 Ga if the default mantle-crust transfer coefficient D_W of 200 is used (Fig. 9a). Prolonging the time interval of $\mu^{182}W_{UM}$ ~ +10 and +15 therefore also requires a higher W flux to the crust, resulting in a higher Hf/W ratio in the UM, and consequently, an increased W flux with positive $\mu^{182}W$ back into the UM. Such a higher W flux to the crust is simulated by increasing the mantle-crust D_W from 200 (Fig. 9a) to ~400, and is used for the models shown in Figure 8 and 9b, which reproduce the target range of $\mu^{182}W_{UM}$ ~+10–15 in the Archean. Similar ^{182}W evolution

patterns in mantle reservoirs are also observed for core formation periods of 30 Myr (Fig. S5), 60 Myr (Fig. S6), and 100 Myr (Fig. S7).

Adding a larger fraction of the total amount of LAM to the UM, for example 10%, leads to a steep decline from $\mu^{182}W_{UM}$ >+20 at the beginning, to ~0 at the end of the late accretion period at 3.8 Ga, which is shown in Fig. 9a for a D_W of 200. Increasing the D_W from 200 to 400 in this case does not compensate for the $\mu^{182}W_{UM}$ ~0 at the end of the late accretion period (not shown), and thus such a larger fraction of LAM to the UM cannot reproduce the target range of $\mu^{182}W$~ +10 to +15 in the UM.

3.4.3 Variable rates of late accretion

Positive $\mu^{182}W_{UM}$ between ~+10 to +15 in Archean rocks require a mantle reservoir that receives only a small fraction of the total LAM, which in our model is the UM. How the LAM is distributed per time interval, i.e., the rate of late accretion, only has a second-order effect on the $\mu^{182}W$ evolution of the UM.

Several different scenarios are explored (Fig. 6), for example a high flux initially or late, which simulates accretion of single large bodies. In case of a high flux early in the late accretion period, 90% of the total amount of LAM is added non-uniformly to the mantle in the first 100 Myr after the core formation, whereas the remaining 10% is added to the mantle thereafter until 3.8 Ga (from the total, 2% added to UM and 98% to the LM as in Fig. 8). In this case, $\mu^{182}W_{UM}$ decreases from values >+25 to values <+10 in the time interval between 4.0 and 2.5 Ga (Fig. 6c) and therefore does not reproduce the target range of +10 to +15 in this time-period. For delayed late accretion or a high flux towards the end of the late accretion period, only 10% of the total amount of LAM is added to the mantle until 3.9 Ga and the remaining 90% of the material is added in the last 100 Myr of the late accretion period between 3.9 and 3.8 Ga. In this case, the $\mu^{182}W_{UM}$ suddenly decreases from +26 at 3.9 Ga to ~0 at 3.8 Ga (Fig. 6c), but thereafter increases towards a positive value due to addition of recycled crust with $\mu^{182}W$ >0, and maintains $\mu^{182}W_{UM}$ ~+10–15 only for the second half of the late accretion period.

These results show that reproducing the observed excess ^{182}W in Archean rocks requires uneven distribution of the LAM between different mantle reservoirs, that is, heterogeneous rather than homogeneous late accretion. Although the rate of late accretion also influences the $\mu^{182}W$ evolution of the silicate reservoirs, the mass fluxes associated with concurrent crust formation and recycling back into the mantle dominate the W distribution and therefore determine how sensitive the ^{182}W isotope evolution of the crust and different mantle reservoirs is to the amount of LAM in each time interval (Fig. 6). The most plausible $\mu^{182}W_{UM}$ evolution that reproduces the observed $\mu^{182}W$~+10–15 from ca. 4.0 to 2.5 Ga in Archean rocks is for addition of only ~2% of the total amount of LAM to the UM with a constant late accretion rate, and the remainder going to the LM (Fig. 6).

3.5 ^{146}Sm–^{142}Nd isotopic evolution

Samarium and Nd are lithophile elements, and thus the $^{142}Nd/^{144}Nd$ and $^{143}Nd/^{144}Nd$ isotope evolution is not affected by core formation. The model results for various core formation periods therefore represent the initiation of silicate differentiation at different times after solar

system initial (Fig. 10, Fig. S8). The μ^{142}Nd evolution in all the terrestrial reservoirs in our model is also not affected by late accretion, because the Sm/Nd (^{146}Sm/^{144}Sm, ^{147}Sm/^{144}Sm, and ^{147}Sm/^{144}Nd) of the late accreted material (Supplementary Table S4) and the mantle are assumed to be chondritic and contribute only a negligible amount of the BSE's Sm-Nd budget. Therefore, deviations from $\mu^{142}\text{Nd} \neq 0$ in the presented model result from silicate differentiation only, that is, incompatible element depletion and enrichment of the various mantle reservoirs (UM, LM, IR) in response to formation and recycling of the CC.

Assuming the same model parameters that reproduced the ^{182}W isotopic evolution in the mantle (Fig. 8) and assuming the same D_{Sm} and D_{Nd} values adopted by Kumari et al. (2016 and 2019) that successfully reproduced the long-lived ^{147}Sm–^{143}Nd systematics, the μ^{142}Nd of all modeled mantle reservoirs remains within the range of the present BSE composition (Fig. 10a, Fig. S8; $\mu^{142}\text{Nd}_{\text{BSE}} = 0 \pm 5.6$; e.g., Rizo et al., 2013). In contrast, μ^{142}Nd in mantle-derived rocks reach a maximum value of +17.5 by the end of the Hadean (4.0 Ga, Rizo et al., 2013) and +11 by the end of the Eoarchean (3.6 Ga, Saji et al., 2018). These positive ^{142}Nd anomalies in mantle-derived rocks generally disappear after ~2.5 Ga, suggesting homogenization of ^{142}Nd signatures in Earth's mantle by the end of the Archean (e.g., Caro, 2011; Rizo et al. 2013, Carlson et al., 2019), similar to what is observed for the ^{182}W evolution (Rizo et al., 2016; Mundl et al., 2018; Rizo et al., 2019).

One way to achieve positive μ^{142}Nd values in the presented model, similar to what is observed in Archean mantle-derived rocks, is to restrict the recycling flux from the CC to the UM. Less recycling of CC into the UM should lead to more positive $\mu^{142}\text{Nd}_{\text{UM}}$. However, crustal recycling during the Hadean and Archean is essential for reproducing the ^{143}Nd isotopic evolution in our previous studies (Kumari et al., 2016, 2019), in good agreement with the results of Jones et al. (2019) and Rosas and Korenaga (2018). It is also required to maintain the $\mu^{182}\text{W}_{\text{UM}}$ ~+10–15 during the entire Archean (Section 3.2). Producing significantly positive $\mu^{142}\text{Nd}_{\text{UM}}$ values by restricting the recycling flux to the mantle reservoirs in the model is therefore problematic.

Another parameter that affects the extent of Nd depletion in the UM is its relative mass (m_{UM}). The mass of the UM in the presented model increases to ~60% of the entire mantle at present (i.e., $m_{\text{UM}} = 0.6$). This is consistent with the mass-balance of heat producing elements (Turcotte et al., 2001; Arevalo et al., 2013) and the mass flux from the LM to the UM in our model, which is scaled to match the present plume flux (see Kumari et al., 2016, 2019 for a more detailed discussion of this aspect). The long-lived isotope systematics evaluated in our earlier models (Kumari et al., 2016, 2019), however, allow for some flexibility in the present value for the m_{UM}. Decreasing the present m_{UM} value but maintaining the same rate of crustal growth (see section 2.1, Kumari et al., 2016, 2019) effectively leads to the extraction of the same amount of CC from a relatively smaller fraction of the UM, and thus greater depletion of Nd in the UM. For example, decreasing m_{UM} from 0.6 to 0.4 considerably changes the evolution of μ^{142}Nd and ε^{143}Nd in the UM, CC, and IR, but leads to a negligible change in the LM for silicate differentiation starting 45 Myr after Earth formation (Fig. 10b and Fig. S9). Compared to $m_{\text{UM}} = 0.6$, assuming $m_{\text{UM}} = 0.5$ results in a $\mu^{142}\text{Nd}_{\text{UM}}$ of +3.6, and a higher $\mu^{142}\text{Nd}_{\text{UM}}$ of +5.6 during the Hadean (Fig. 10b). Although $\mu^{142}\text{Nd}_{\text{UM}}$ of +11.5 is achieved in the Hadean for

m_{UM} = 0.4, m_{UM} <0.5 cannot reproduce the $^{182}Hf–^{182}W$ systematics in our model, which limits the plausible values for m_{UM}. For m_{UM} = 0.5, but slightly higher D_{Sm} and D_{Nd} values than assumed by Kumari et al. (2016; Fig. 10a-b; Table 3 case I), our model generates a $\mu^{142}Nd_{UM}$ of ~ +11 by the end of the Hadean and Eoarchean (Fig. 10c, Table 3 case II). The resulting $\varepsilon^{143}Nd$ evolution in the terrestrial reservoirs also satisfies the present constraints (Fig. S9; Table 3).

Interestingly, varying the residence time of recycled CC in the IR from 10 Myr to 5000 Myr, and therefore mimicking either complete mixing of the recycled crust with the LM or the formation of an isolated crustal reservoir, leads to no significant variation in the $\mu^{142}Nd$ of the crust and mantle reservoirs, except for the latter case where the IR evolves to a present $\mu^{142}Nd$ of ~ –10 (Fig. 10a). These results are in principal agreement with the mass balance discussed by Boyet and Carlson (2005), who concluded that an early-formed, and subsequently isolated crustal reservoir must be much more incompatible element enriched than the current continental crust (the CC reservoir in our model) or, almost the entire mantle must have been involved in Hadean crust formation to develop $\mu^{142}Nd \neq 0$ of the accessible silicate Earth.

4. DISCUSSION

4.1 Constraints on the rate of core formation

In our model, different mass and associated W flux rates to the core are achieved by changing the bulk silicate-metal transfer factor, $D_{W,silicate\text{-}metal}$ (Table 4 and Table S5). These different W flux rates to the core determine the pre-late accretion $\mu^{182}W_{BSE}$, W_{BSE}, and Hf/W_{BSE} values for different core formation periods and have the principal control on the amount of LAM necessary to evolve to $\mu^{182}W_{BSE} = 0$ (section 3.1).

In previous models (e.g., Halliday et al., 1996; Harper and Jacobsen, 1996; Kleine et al., 2004; Rudge et al., 2010; Fischer and Nimmo, 2018), the $\mu^{182}W_{BSE}$, W_{BSE}, and Hf/W_{BSE} values at the end of core formation are regulated by several parameters during early accretion and core formation processes. Other than the duration of core formation, these are the rate of accretion, the type of accreting material (differentiated or undifferentiated bodies), the extent of metal-silicate equilibration of the accreting (differentiated) material, and the partitioning of W between metal and silicate. None of these parameters, however, is well constrained. A wide range of underlying parameters (e.g., accretion rate, metal silicate equilibration rate, accretion of differentiated or undifferentiated bodies), and thus early accretion and core formation scenarios is therefore compatible with the isotopic constraints (Rudge et al., 2010). But any combination of these diverse parameters effectively sets the W concentration (Hf/W ratio) and $\mu^{182}W$ of the BSE at the end of core formation. Although simplified, the same result is achieved in our model by varying the bulk silicate-metal transfer factor for W ($D_{W,silicate\text{-}metal}$), which effectively allows investigating a wide range of core formation scenarios.

Notably, the $D_{W,silicate\text{-}metal}$ used in our model is different from the W partition coefficient between metal and silicate ($K^d_{W,metal/silicate}$). However, our model-derived concentrations in the core and BSE (Table 2) can be used to calculate an effective $K^d_{W,metal/silicate}$ for variable core formation periods, and core formation scenarios. Assuming linear core growth, the calculated $K^d_{W,metal/silicate}$ is 11.5 for t_{CF} = 30 Myr, 23 for t_{CF} = 45 Myr, 46 for t_{CF} = 60 Myr, and 331 for

t_{CF} = 100 Myr (see supplementary material section 1). In comparison, the $K^d_{W,metal/silicate}$ inferred in previous studies ranges from ~17 to ~200 (Wade and Wood, 2005; Kleine and Walker, 2017). Therefore, although the $D_{W,silicate-metal}$ in our model is essentially a free parameter allowing for a wide range of possible core formation scenarios, calculating $K^d_{W,metal/silicate}$ values from the W concentrations in the core and BSE at the end of core formation allows comparing our model results to those of more complex core formation models, and thus narrowing down the plausible range of scenarios. Assuming linear core growth, for example, the calculated $K^d_{W,metal/silicate}$ values are in good agreement with literature values (Wade and Wood, 2005; Kleine and Walker, 2017) for t_{CF} ~ 30-80 Myr (see more detailed discussion in the supplementary materials).

Hence, the key parameters that determine the $\mu^{182}W_{BSE}$, W_{BSE}, and Hf/W_{BSE} values at the end of core formation in our, and previous more elaborate core formation models, are the timing and rate of core formation and associated W flux to the core (Table 4). The continuous, linear core formation rate used in our default model is considered a median case. In this case, core formation times between 40-60 Myr result in W_{BSE} and Hf/W_{BSE} values within the estimated range (W_{BSE} = 13 ± 10, Arevalo and McDonough, 2008; Hf/W_{BSE} = 17± 5, Kleine et al., 2009; Table 4, Fig. 11).

The W_{BSE} (Hf/W_{BSE}) at the end of core formation, however, depends more strongly on the rate rather than the total duration of core formation (section 3.1 and 3.2; Fig. 11). The W_{BSE} (and $\mu^{182}W_{BSE}$) increase and the Hf/W_{BSE} decrease for progressively larger W flux rates to the core early during a given core formation period (Fig. 3 and 11). Even for a core formation time of 100 Myr, where the W_{BSE} is excessively low (and thus Hf/W_{BSE} unrealistically high) for a linear core formation rate (Table 4; Fig. 11), W_{BSE} and Hf/W_{BSE} within the range of current estimates can thus be found by varying the core formation rate. If more than 50% of the W is transferred to the core within the first 30 Myr of the 100 Myr core formation period, for example, the resulting W_{BSE} and Hf/W_{BSE} are within the range of current estimates (Table S5; Fig. 11). There is a limit, however, on the rate of early core formation. Models where 90% of the W goes into the core in the first 10 Myr of core formation all have very similar, but excessively high W_{BSE} (low Hf/W_{BSE}) independent of the total duration of core formation (Table 4; Fig. 11).

Overall, therefore, it is mostly the rate of core formation, rather than the total duration of core formation that influences the $\mu^{182}W_{BSE}$, W_{BSE}, and Hf/W_{BSE} values at the end of core formation. The W_{BSE} is very sensitive to this effect, and becomes much lower (Hf/W_{BSE} higher) if a large fraction of the W is transferred to the core in the second half of a given core formation period. Compare, for example, the W_{BSE} (Hf/W_{BSE}) for variable rates of core formation for t_{CF} = 100 Myr in Table S5 and Fig. S3. Hence, single events, for example a giant impact, which cause large, sudden mass fluxes to the core also have a large influence on the $\mu^{182}W_{BSE}$, W_{BSE}, and Hf/W_{BSE} values at the end of core formation. Such scenarios are captured by our models where 90% of the W enters the core in the first or last 10 Myr of core formation (Table 4). Excessively high W_{BSE} (low Hf/W_{BSE}) result for rapid early core growth, and low W_{BSE} (high Hf/W_{BSE}) for late core growth, independent of the duration of core formation. A giant impact

shortly before the end of a 100 Myr (or longer) core formation period, for example, is therefore difficult to reconcile with current estimates of the W_{BSE} and Hf/W_{BSE} values (Table 4; Fig. S3).

Overall, the discussion above shows that more precise constraints on W_{BSE} would provide tighter constraints on several key, but largely unconstrained processes, such as the duration and rate of core formation, the timing of a giant, moon-forming impact during the pre-late accretion phase, but also the amount of late accreted material, as discussed in the following.

4.2 Constraints on the amount and type of late-accreted material

Addition of variable amounts of LAM decreases the $\mu^{182}W_{BSE}$ to 0 by the end of the late accretion period (3.8 Ga, Fig. 4). As discussed in sections 3.2 and 4.1 and shown in Figs. 3-5 (Table 4), the amount of LAM depends mostly on the W_{BSE} at the end of core formation. For the default linear core formation model, W_{BSE} at the end of core formation (38-1.5 ppb) and the amount of LAM (1.9-0.07%) decreases with increasing duration of core formation (Figs. 3 and 4; Table 4). However, the rate of core formation has a large influence on the W_{BSE} (Hf/W_{BSE} and $\mu^{182}W_{BSE}$) at the end of core formation and thus also the amount of LAM inferred from the ^{182}W systematics. Consequently, an even larger range of W_{BSE} (68–0.09 ppb) and amount of LAM (3.4–0.004%) results, even for a fixed duration of core formation (e.g., 100 Myr), but variable rates of core growth (or rate of W transfer to the core, Table 4, Table S5; Fig. S3).

Nevertheless, the amount of LAM inferred from the ^{182}W isotope systematics in our model (Table 4; Fig. 4) is generally in good agreement with HSE-based estimates. However, the rate of core formation and the amount of LAM are mutually dependent on W_{BSE}, that is, estimates of the amount of LAM based on ^{182}W isotope constraints are only possible for a given rate and overall duration of core formation. Because a wide range of (early accretion and) core formation scenarios in our and previous models (e.g., Halliday et al., 1996; Harper and Jacobsen, 1996; Kleine et al., 2004; Rudge et al., 2010; Fischer and Nimmo, 2018) are compatible with current constraints on W_{BSE} (13 ± 10, Arevalo and McDonough, 2008) and Hf/W_{BSE} (17± 5, Kleine et al., 2009), the ^{182}W isotope systematics alone do not allow tight constraints on the amount of LAM (Fig. 5), until more precise estimates of the W_{BSE} become available.

Notably, the amount of LAM inferred from our model (Table 4; Fig. 4) is derived for a single composition of the LAM (section 2.4). Considering variability in the W concentration and/or isotope composition of the late accreted material, for example by accreting differentiated versus undifferentiated bodies, certainly influences the amount of LAM, but only within the bounds set by the core formation (and early accretion) processes (section 3.2). Late accretion contributes only ~7–13% of the W budget of the BSE in our models (Table 4), which is consistent with other estimates (e.g., Kleine and Walker, 2017). The present elemental and ^{182}W budget in the silicate Earth (W_{BSE} and $\mu^{182}W_{BSE}$) is therefore mostly set during the pre-late accretion phase. Considering variability in the type of LAM (e.g., differentiated vs. undifferentiated bodies) is thus certainly important, especially for reconciling constraints on the amount and type of LAM from the HSE budget and the ^{182}W isotope evolution, but is of

subordinate importance for constraining the amount of LAM from the ^{182}W isotope constraints alone.

The effect of differentiated (e.g., Marchi et al., 2018) versus undifferentiated (as assumed in our modeling study) nature of late accreting bodies on the Hf-W isotopic evolution of Earth needs to be evaluated. In order to be compatible with the HSE, Re-Os, and moderately-volatile-chalcophile element (e.g., Se-Te) constraints, Kruijer et al. (2015) suggest a carbonaceous-chondrite-like LAM composition with a minor fraction of iron-meteorite-like material. Note that our bulk-Earth-like LAM μ^{182}W and W concentrations are similar to Kruijer et al. (2015). Different chondrite groups have very similar μ^{182}W and W concentrations (e.g. Kleine et al., 2004) and chondrites constitute 80% of the mix of LAM favored by Kruijer et al. (2015). The μ^{182}W and W concentrations of the LAM vary mainly by changing the proportion of chondrite to iron meteorite (IV A group has 10 times higher W and μ^{182}W = –350). But because of the fractionated HSE patterns of the iron meteorites, there is limited flexibility on the chondrite/iron meteorite ratio (Day et al., 2016; Walker et al., 2008; McCoy et al., 2011). Therefore, the associated variation in bulk μ^{182}W and W compositions of the LAM is comparatively small and has a second-order effect on the amount of LAM and thus the μ^{182}W evolution of the silicate Earth during the late accretion phase.

However, if a large fraction of the LAM were differentiated material (Marchi et al., 2018), the bulk μ^{182}W and W composition of the accreted differentiated material could change significantly depending on how much of the impactor's core was retained in (or equilibrated with) Earth's mantle. According to simulations by Marchi et al. (2018), ~20-70% of the impactor's core are retained in Earth's mantle depending on impactor's size, angle and velocity. Taking μ^{182}W and W compositions of core and mantle of impacting differentiated body from Marchi et al. (2018), the bulk impactor composition changes considerably, ranging from μ^{182}W = +26 and W = 45 ppb for retaining 20% of the impactor's core to μ^{182}W = –163 and W = 120 ppb for retaining 70% of the impactor's core, the latter is similar to our LAM. Thus, depending on the composition of impactors, its size, and impact conditions, late accretion of differentiated bodies may introduce much more heterogeneous material with respect to μ^{182}W and W composition than accreting undifferentiated bodies. In this case the effect of late accretion on μ^{182}W and W composition of Earth is difficult to predict due to an enormous range of free parameters (impactor's size, fraction core retained, impact conditions, etc.) and thus any modeled scenario would be highly speculative. We did not include any specific model of differentiated impactor for this reason. Moreover, metal distribution and/or metal-silicate equilibration may be limited to localized domains (Marchi et al., 2018, Maas et al., 2021) and create considerable (transient?) heterogeneity in μ^{182}W with either higher or lower μ^{182}W than the terrestrial mantle at the time of impact.

4.3 Impact of present pre-late accretion $\mu^{182}W_{BSE}$ on the amount of late-accreted material

Varying the assumed present, pre-late accretion value of $\mu^{182}W_{BSE}$ = +25 influences the modeled μ^{182}W evolution of the BSE. This value is estimated by subtracting LAM from the present BSE with $\mu^{182}W_{BSE}$ = 0 (e.g., Kruijer et al., 2015; Touboul et al., 2015). With a mass and composition of the LAM constrained by the HSE systematics (e.g., Day et al., 2007;

Walker, 2009; Fischer-Gödde and Becker, 2012), and current estimates for the W_{BSE} (Arevalo and McDonough, 2008), the resulting present pre-late accretion $\mu^{182}W_{BSE}$ varies between +10 and +40 (Kruijer et al., 2015; Touboul et al., 2015).

A different present pre-late accretion $\mu^{182}W_{BSE}$ leads to a different ^{182}W evolution of the BSE. As discussed in detail in sections 3.1 and 3.2, the latter is controlled by the parameters listed in equation (2). That is, the $\mu^{182}W_{BSE}$ at t_{CF} ($^{182}W/^{184}W_{BSE,\,tCF}$), as well as the Hf/W_{BSE} and $^{182}Hf/^{180}Hf$ at t_{CF}. These parameters, and thus the present pre-late accretion value for $\mu^{182}W_{BSE}$, are controlled by the rate and duration of core formation (and early accretion). The ratio $^{182}Hf/^{180}Hf$ is entirely controlled by time, i.e., the duration of core formation (t_{CF}), whereas the $\mu^{182}W_{BSE}$ and Hf/W_{BSE} at t_{CF} are mostly influenced by the rate of core formation. Because Hf/W_{BSE} is determined by W_{BSE}, which is the main parameter that controls the amount of LAM, a different ^{182}W evolution of the BSE also affects the amount of LAM (sections 3.1 and 3.2). Early rapid rates of core growth for a given t_{CF}, for example, lead to high $\mu^{182}W_{BSE}$ at t_{CF}, but low Hf/W_{BSE} due to high W_{BSE} (Table 4). Achieving higher present, pre-late accretion $\mu^{182}W_{BSE}$ in this way therefore requires larger amounts of LAM to decrease $\mu^{182}W_{BSE}$ to 0 (and vice versa). Several quantitative examples, showing to what extent the amount of LAM is affected by different $^{182}W_{BSE}$ evolution resulting from variable present pre-late accretion $\mu^{182}W_{BSE}$ values are given in the supplementary material (Tables S6 and S7). These examples show that the amount of LAM is affected considerably by assuming a different $^{182}W_{BSE}$ evolution, but on a similar order as by varying the duration and rate of core formation. Hence, the interdependency of $\mu^{182}W_{BSE}$ and Hf/W_{BSE} (W_{BSE}) at t_{CF} on the amount of LAM make it impossible to constrain the amount of LAM from the ^{182}Hf–^{182}W isotope systematics alone without constraining the duration and rate of core formation. Figure 12, for example, shows that even for a given amount of LAM, e.g., constrained by the HSE systematics, a given value for W_{BSE} (Hf/W_{BSE}), as well as present pre-late accretion $\mu^{182}W_{BSE}$, the ^{182}Hf–^{182}W isotope systematics are compatible with a range of $\mu^{182}W_{BSE}$ at t_{CF}, i.e., principally permit many possible combinations of duration and rate of core formation (Fig. 12; Table 4; cf. Rudge et al., 2010). Notably, this large possible range of $\mu^{182}W_{BSE}$ at the end of core formation (cf. Halliday et al., 1996; Harper and Jacobsen, 1996; Kleine et al., 2004) complicate constraining the ^{182}Hf–^{182}W evolution of the Earth-Moon system even for tight constraints on the initial lunar $\mu^{182}W$ value (cf. Kruijer et al., 2015; Touboul et al., 2015; Kruijer and Kleine, 2017; Maurice et al., 2020).

Owing to the interdependency and considerable uncertainty of the present pre-late accretion $\mu^{182}W_{BSE}$, W_{BSE} (Hf/W_{BSE}), and the amount of LAM (sections 3.1 and 3.2), the ^{182}Hf–^{182}W evolution of the Earth-Moon system remains underdetermined. Reducing the uncertainty on the present W_{BSE} (13 ± 10, 2SD; Arevalo and McDonough, 2008) however, would narrow down the target range for W_{BSE} (Hf/W_{BSE}) of core formation models, and thus also the present, pre-late accretion $\mu^{182}W_{BSE}$ value, and would also allow constraining the amount of LAM more precisely. Deriving more precise constraints on the present W_{BSE} therefore, is key for improving our understanding of core formation processes, and the ^{182}Hf–^{182}W evolution of the Earth-Moon system.

4.4 The rate and style of late accretion and its admixing to the mantle

Archean komatiites (4.0 to 2.4 Ga) with variable HSE abundances (~50-65%) relative to the modern mantle have μ^{182}W roughly between +10 and +15 (Willbold et al., 2011, 2015; Touboul et al., 2012; Rizo et al., 2016; Dale et al., 2017; van de Löcht et al., 2018). The 3.55 Ga Schapenburg komatiites are an exception with μ^{182}W of –8.4 ± 4.5 (2SD) and lower HSE abundances than the modern mantle (Puchtel et al., 2016). Similarly, a recent study by Puchtel et al. (2020) reported a μ^{182}W of ~ –10 for the source of ~2.05 Ga old Jeesiörova and Kevitsa komatiites from the Central Lapland Greenstone Belt, Finland, which seemingly derived from a source containing ~120 ± 5% of HSE budget of the present BSE. However, the long-lived radiogenic isotope systematics of most Archean komatiites and post-Archean mantle-derived basalts generally indicate derivation from a variably incompatible element depleted mantle (e.g., ε^{143}Nd ≥0), and thus our model simulations aimed for a range of $\mu^{182}W_{UM}$ of +10 and +15 between 4.0 and 2.5 Ga in the modeled UM reservoir (e.g., Fig. 8).

For homogeneous late accretion, none of the modeled mantle reservoirs achieve the target range of μ^{182}W ~+10 to +15 in the mantle between 4.0 and 2.5 Ga (section 3.2). Adding LAM to both the UM and LM in the same relative proportions for a period of 760 Myr (until 3.8 Ga) results in $\mu^{182}W_{UM}$ <0 throughout the Archean for core formation periods of 30–100 Myr (Fig. 7). This corresponds to a geodynamic scenario where the LAM was quickly distributed and homogenized throughout the entire mantle (uniform mixing) until the end of the abundant lunar cratering period (e.g., Tera et al., 1974; Kring and Cohen, 2002). In this scenario, $\mu^{182}W_{UM}$ <0 takes until after 2.0-1.5 Ga to dissipate and approach μ^{182}W ~0 (Fig. 7). In the LM reservoir, μ^{182}W values >>15 result before 3.8 Ga and steeply decrease to ~0 in the early Archean, and thereafter remain nearly constant until the present (Fig. 7). But the modeled LM retains μ^{142}Nd and ε^{143}Nd ~0 (Fig. 10 and Fig. S8 and S9), and thus could only explain Archean komatiites with μ^{182}W >0, but μ^{142}Nd ~0 and ε^{143}Nd ~0 before ~3.5 Ga (e.g., Willbold et al., 2011, Rizo et al., 2016; Archer et al., 2019) or μ^{182}W ~0 and μ^{142}Nd = ε^{143}Nd ~0 after ~2.5 Ga (Rizo et al., 2013; Mundl et al. 2018; Rizo et al., 2019).

Therefore, maintaining $\mu^{182}W_{UM}$ in the range of +10 to +15 requires that the total amount of LAM added to parts of the mantle, the UM in our model, is comparatively small (2% of the total late accretion flux, Fig. 8). This corresponds to a geodynamic scenario where the impactors are not efficiently homogenized within the entire mantle but are distributed and/or equilibrated with only parts of the mantle, similar to what has been suggested by ^{182}W studies of Archean rocks (Willbold et al., 2011; 2015; Dale et al., 2017; Archer et al. 2019).

Variable flux rates of LAM in different time intervals during the entire late accretion period (early rapid, delayed or linear fluxes) also affect the evolution of $\mu^{182}W_{UM}$ (Fig. 6). A large flux early in the late accretion period fails to produce the $\mu^{182}W_{UM}$ of +10 to +15 for a prolonged time period, but either a delayed or linear late accretion model (or a constant flux of late accretion to mantle) successfully reproduce the $\mu^{182}W_{UM}$ of +10 to +15 from 4 to 2.5 Ga (Fig. 6c). Although the rate of late accretion therefore influences the μ^{182}W evolution of the silicate reservoirs, the mass fluxes associated with concurrent crust formation and recycling back into the mantle dominate the W distribution and thus the ^{182}W isotope evolution of the crust and different mantle reservoirs (compare Fig. 6b, c and d).

4.5 Timing of early silicate differentiation

Observed μ^{142}Nd excesses in Archean komatiites are crucial evidence for the onset of mantle depletion in response to crust formation in the Hadean. The ubiquitous presence of μ^{142}Nd excess (μ^{142}Nd ~+15) in 3.8–3.7 Ga old rocks from the Isua Supracrustal Belt suggests that the source mantle must have acquired this ^{142}Nd excess during the Hadean, implying silicate differentiation starting ~4.5 Ga (Caro et al., 2006; Boyet and Carlson, 2006; Bennett et al., 2007; Rizo et al., 2011, 2013; Rizo et al. 2016; O'Neil et al., 2016; Saji et al., 2018). Similar ^{142}Nd excess (μ^{142}Nd: +5 to +15) are also identified in other ancient terrains such as the Yilgarn Craton in Western Australia (3.7 Ga; Bennett et al., 2007) and the Abitibi Greenstone Belt in Canada (2.7 Ga; Debaille et al., 2013).

However, the model parameters that successfully reproduce the nearly constant target ^{182}W signatures in the UM do not result in significant μ^{142}Nd excesses in the modeled UM (Fig. 10a), which would be required to explain the combination of μ^{182}W ~+10–15 and μ^{142}Nd >0 observed in many Archean komatiites (Willbold et al., 2011; Rizo et al., 2016). More positive μ^{142}Nd of ~+11 by the end of Hadean can be achieved in the presented model in two ways: (1) increasing the elemental enrichment factors (D_{Sm} and D_{Nd}), thus more efficient transfer of Sm and Nd from the UM to the CC and/or, (2) decreasing the fraction of present depleted mantle (m_{UM}) from which 90% of the crust is being formed, thus effectively extracting the same amount of CC from a smaller mass of UM. Both parameters are varied such that μ^{142}Nd of ~+11 by the end of Hadean can be achieved. The required D_{Sm} and D_{Nd} (Table 3, case II) and m_{UM} = 0.5 are slightly different from the values assumed in Kumari et al. (2016, 2019), but consistent with the ^{143}Nd and ^{182}W evolution in the crust-mantle system (Figs. 13 and S9). Figure 13, for example, shows the effect of m_{UM} (0.6→0.5) on the evolution of ^{182}W, where the $\mu^{182}\mathrm{W}_{\mathrm{UM}}$ at the end of late accretion is slightly less positive due to addition of same amount of LAM for a smaller relative UM mass, but the target +10 to +15 during the Archean is still reproduced (see Fig. S9 for the ^{147}Sm–^{143}Nd evolution).

Therefore, both the modeled ^{182}Hf–^{182}W systematics and ^{142}Nd (^{143}Nd) data on Archean komatiites require that formation of differentiated crust (low Sm/Nd and Hf/W) and mantle (high Sm/Nd and Hf/W) initiated soon after core formation. A delay in silicate differentiation, for example after the first 100 Myr, results in a maximum $\mu^{142}\mathrm{Nd}_{\mathrm{UM}}$ of ~+5 by the end of the Hadean, similar to the present value. Delayed crust formation, particularly after the life-time of ^{182}Hf, would also affect the $\mu^{182}\mathrm{W}_{\mathrm{UM}}$ evolution, because this would limit both the $\mu^{182}\mathrm{W}_{\mathrm{CC}}$ to less positive values and the amount of crustal return flux into the UM, thus making it difficult to protract the time interval of $\mu^{182}\mathrm{W}_{\mathrm{UM}}$ ~+10 to +15 for the entire Archean (4.0–2.5Ga). Our model therefore suggests that a significant amount of early crust formation, within the life-time of ^{182}Hf, and its subsequent recycling is essential for reproducing the variable, but often decoupled μ^{182}W and μ^{142}Nd signatures in Archean rocks.

The box-model by Rosas and Korenaga (2018) also indicates rapid continental crust formation in the early Hadean, creating as much as the present volume of continental crust by the end of the Hadean. The extensive mantle depletion in the Hadean, in response to the massive crustal growth in the model of Rosas and Korenaga (2018) produces an average μ^{142}Nd ~+15

in the upper mantle, close to the maximum value measured thus far in Archean rocks (μ^{142}Nd = +17.5; Rizo et al., 2013). If taken as the average of a distribution of values around the mean, the lower average $\mu^{142}Nd_{UM}$ ~+11 in our model is in principal agreement with the more positive μ^{142}Nd values observed on some of the Archean rocks, and permit more moderate crustal growth rates in the Hadean compared to the model by Rosas and Korenaga (2018).

In general, once the short-lived systems become extinct, recycling of crustal material and its mixing in the convective mantle removes the early-formed isotopic anomalies by the end of the Archean (for ^{142}Nd) and drives the ^{182}W–^{142}Nd isotopic compositions of the crust and mantle reservoirs towards $\mu^{142}Nd_{BSE}$ ~0 and $\mu^{182}W_{BSE}$ ~0.

4.6 Implications for the μ^{182}W–μ^{142}Nd systematics in Archean rocks

The reason for decoupling the μ^{182}W and μ^{142}Nd signatures in Archean rocks is that although crust-mantle exchange affects both systems in the same sense, the ^{182}Hf–^{182}W isotope evolution of the BSE is significantly affected by core formation and thereafter modified by late accretion, but the Sm–Nd system is not. In the presented model, the UM has positive values for both μ^{182}W and μ^{142}Nd in the Archean (Fig. 8, Fig. 10c, see also Fig. S4 for core formation times of 30, 60 and 100 Myr), in good agreement with what is observed for the 3.8–3.3 Ga old rocks from the Isua Supracrustal Belt, Greenland (Willbold et al., 2011; Rizo et al., 2016). The μ^{182}W >0 but μ^{142}Nd ≈0 for the 3.45–3.3 Ga rocks from Pilbara Craton, Western Australia (Archer et al., 2019), can be explained by a more moderately depleted mantle, which still preserves the positive μ^{182}W (Fig. 8), but develops no significant μ^{142}Nd anomalies (Fig. 10a). A positive μ^{182}W and negative μ^{142}Nd is observed in the modeled CC (Figs. 8 and 10c), suggesting that the μ^{182}W >0 and μ^{142}Nd <0 in the 4.0–3.6 Ga old rocks from the Acasta Gneiss Complex, Canada (e.g., Roth et al., 2014; Willbold et al., 2015; Reimink et al., 2018) are inherited crustal signatures. The coupling of negative μ^{142}Nd and μ^{182}W observed in the 3.55 Ga old Schapenburg komatiites (Puchtel et al., 2016), are more difficult to explain within the context of the presented model, because no single reservoir has both μ^{142}Nd and μ^{182}W <0 at any given time (Figs. 8 and 10). These rocks therefore likely have a more complex, multi-stage history, and perhaps acquired or inherited their μ^{142}Nd and μ^{182}W signatures during different phases of their evolution (Puchtel et al., 2016).

4.7 Implications for μ^{182}W deficits in modern OIBs

Several studies have reported negative μ^{182}W (−5 to −23) in plume-derived ocean island basalts (OIB, Mundl et al., 2017; Rizo et al., 2019; Mundl-Petermeier et al., 2020). This observed ^{182}W-depletion in some modern OIBs can be explained within the framework of our model if part of the recycled CC remains isolated for most of Earth's history; see the evolution of the IR for an isolation time of 5000 Myr in Fig. 8 and Fig. S4. The IR in our model is essentially a storage container for part of the recycled continental crust. As such, the IR could either be perceived as an isolated part of the continental crust, or an isolated reservoir of recycled CC in the mantle, although it is probably difficult to store low-density crust enriched

in incompatible and heat producing elements such as Th, U and K for sufficiently long time periods at a mantle boundary layer (e.g., the core-mantle boundary).

Nevertheless, for a residence time of the recycled CC in the IR of 5000 Myr, there is no material exchange between the IR and LM, allowing the LM to retain a ^{182}W-deficit acquired during late accretion. Consequently, $\mu^{182}W_{LM}$ develops and maintains approximately constant values of –6.9 (t_{CF} = 30 Myr) and –5.8 (t_{CF} = 60 Myr) from the end of late accretion to the present (Figs. 8 and S4), despite significant mass transfer from the LM to the UM (and from the CC to the UM and LM). Hence mantle plumes originating from a mantle reservoir that has received (or equilibrated with) a certain flux of late accreted material but has never incorporated a recycled CC with $\mu^{182}W > 0$, could principally have small ^{182}W-deficits. Note that the LM in our model represents most of the total mantle, especially in the early Archean. As mass fluxes in our model are instantly homogenized within each reservoir, the value for each reservoir at any time should be taken as the average of a distribution of values around the mean. Higher or lower values are therefore implied for each reservoir. Moreover, smaller, natural mantle reservoirs with similar evolution may develop more extreme values than the large reservoirs (or 'boxes') in our model, which may account for the larger range and overall more negative $\mu^{182}W$ values in OIB compared to the modeled range of $\mu^{182}W_{LM}$ in the scenario discussed above.

Alternatively, the ^{182}W deficit in young OIBs have been explained by core-mantle exchange processes (Rizo et al., 2019; Mundl-Petermeier et al., 2020), which would not require preservation of early-formed ^{182}W anomalies in any mantle or crustal reservoir. For example, Rizo et al. (2019) suggested that diffusive exchange at the core-mantle boundary or exsolution of W-rich and HSE-poor Si-Mg-Fe oxides from the outer core to the mantle can modify the $\mu^{182}W$ of the mantle from +20 to about –20. But this would double the HSE abundances, which is inconsistent with the low HSE abundances observed in most OIB with $\mu^{182}W < 0$ (Mundl et al., 2017). Alternatively, Mundl-Petermeier et al. (2020) suggest that equilibration of a (partially) molten silicate layer with the Earth's core could explain the $\mu^{182}W$ deficits in OIB without leading to strongly enriched HSE abundances. Although the exact mechanisms of core-mantle exchange processes remain ambiguous, core-mantle exchange is an attractive way to explain observed ^{182}W deficits in some OIB, because it alleviates the need for preserving early-formed ^{182}W anomalies, which according to the model presented here, is difficult and only possible under special circumstances. Recently, Lesher et al. (2020) argued that thermo-diffusion could lead to iron isotope fractionation across the core-mantle boundary, causing entrainment of fractionated core material into the convecting mantle. Because this scenario would also affect the mantle's $\mu^{182}W$, it should lead to predictable $\mu^{182}W$ and stable Fe isotope variations, and thus be a readily testable hypothesis.

5. CONCLUSIONS

The presented five-reservoir open-system model (Fig. 1) investigates how the ^{146}Sm-^{142}Nd and ^{182}Hf-^{182}W isotope systematics of the silicate Earth are affected by late accretion, and progressive mantle-crust differentiation after core formation. Different rates and durations of core formation result in variable $\mu^{182}W$, Hf/W, and W concentration of the bulk silicate earth

(BSE) at the start of late accretion. The initial $\mu^{182}W_{BSE}$, Hf/W_{BSE}, and W_{BSE} are interdependent parameters and understanding the ^{182}Hf-^{182}W evolution of the silicate earth therefore requires detailed constraints on the timing and rate of core formation and the associated W flux to the core, including the time, composition, and mass flux of a potential moon-forming giant impact. But all these parameters remain major unknowns. It is clear, however, that the rate rather than the total duration of core formation mainly controls the ^{182}Hf-^{182}W systematics, and thus more precise constraints on the rate of early accretion and core formation, and the associated W distribution between silicate and metal are required to narrow down possible range of $\mu^{182}W_{BSE}$, Hf/W_{BSE}, and W_{BSE} values at the start of late accretion.

Ultimately, these different BSE starting values determine the amount of late accreted material required to evolve to $\mu^{182}W_{BSE} = 0$ at the end of the late accretion period, and the ^{182}W evolution of the evolving mantle and crustal reservoirs. The amount of late accreted material is mainly determined by the pre-late accretion W_{BSE} value and thus most sensitive to core formation and early accretion processes. The^{182}W evolution of the evolving mantle and crustal reservoirs is controlled by the proportion of W from the late accreted material to the amount of W in each reservoir. The latter essentially regulates how sensitive each reservoir reacts to the incoming late accretion flux. A progressively depleting mantle with low W concentration is very susceptible to addition of late accreted material with $\mu^{182}W < 0$ (-190), leading to $\mu^{182}W$ deficits, which can only be avoided by limiting the amount of late accreted material. Heterogeneous addition of the late accreted material to Earth's mantle is therefore required to develop variably incompatible element depleted mantle with $\mu^{182}W \geq 0$, as observed in most Archean rocks. Maintaining the near-constant $\mu^{182}W$ ~+10 to +15 observed in mantle-derived rocks throughout the Archean in a progressively more depleted mantle reservoir requires a balance between the addition of late accreted material with $\mu^{182}W < 0$ and recycling of crustal material with $\mu^{182}W > 0$. Although the rate of late accretion also influences the $\mu^{182}W$ evolution of the evolving mantle and crustal reservoirs, it is only a second-order effect, because the mass fluxes between these reservoirs dominate their W concentrations, and because late accretion only contributes ~7–13% of the BSE's W budget.

Notably, reproducing the observed, and often decoupled ^{142}Nd and ^{182}W signatures in Hadean-Eoarchean mantle-derived rocks requires the initiation of continental crust formation, and recycling back into the mantle within the first ~50 Myr after core formation. Due to continuous crust-mantle exchange, these early-formed ^{182}W and ^{142}Nd isotopic anomalies generally disappear in the post-Archean in all silicate reservoirs. However, the recently observed ^{182}W deficits in some young OIBs can be explained within the framework of the presented model by mantle materials that never incorporated a recycled flux of early formed crust with $\mu^{182}W > 0$, and can thus preserve $\mu^{182}W$ deficits acquired during late accretion. Alternatively, the ^{182}W deficits in some young OIBs may result from core-mantle exchange, which would obviate the need for preserving early-formed ^{182}W anomalies, but, of course has very different geodynamic implications.

ACKNOWLEDGEMENTS

Thorsten Kleine is thanked for discussions, especially for pointing out a conceptual mistake in the ^{182}W evolution of earlier models. This work was supported by a research grant (2018/19, 57381333) by the German Academic Exchange Service (DAAD) awarded to Seema Kumari. Seema Kumari also acknowledges support by the Deutsche Forschungsgemeinschaft (DFG, German Research Foundation) – Project-ID 263649064 – TRR 170. This is TRR 170 Publication no. 127. D. Paul acknowledges support from the Science and Engineering Research Board, Govt. of India (Grant # CRG/2018/000045), and from the Alexander von Humboldt Foundation through a renewed research stay award in May-July, 2019.

REFERENCES

Archer G. J., Brennecka G. A., Gleißner P., Stracke A., Becker H. and Kleine T. (2019) Lack of late-accreted material as the origin of ^{182}W excesses in the Archean mantle: Evidence from the Pilbara Craton, Western Australia. *Earth Planet. Sci. Lett.* **528**, 115841. Available at: https://doi.org/10.1016/j.epsl.2019.115841.

Arevalo R. and McDonough W. F. (2008) Tungsten geochemistry and implications for understanding the Earth's interior. *Earth Planet. Sci. Lett.* **272**, 656–665. Available at: http://dx.doi.org/10.1016/j.epsl.2008.05.031.

Arevalo R., McDonough W. F., Stracke A., Willbold M., Ireland T. J. and Walker R. J. (2013) Simplified mantle architecture and distribution of radiogenic power. *Geochemistry, Geophys. Geosystems* **14**, 2265–2285.

Bennett V. C., Brandon A. D. and Nutman A. P. (2007) Coupled ^{142}Nd-^{143}Nd isotopic evidence for hadean mantle dynamics. *Science* **318**, 1907–1910.

Boyet M. and Carlson R. W. (2005) ^{142}Nd evidence for early (>4.53 Ga) global differentiation of the silicate Earth. *Science* **309**, 576–581.

Boyet M. and Carlson R. W. (2006) A new geochemical model for the Earth's mantle inferred from ^{146}Sm-^{142}Nd systematics. *Earth Planet. Sci. Lett.* **250**, 254–268.

Boyet M., Carlson R. W. and Horan M. (2010) Old Sm-Nd ages for cumulate eucrites and redetermination of the solar system initial ^{146}Sm/^{144}Sm ratio. *Earth Planet. Sci. Lett.* **291**, 172–181. Available at: http://dx.doi.org/10.1016/j.epsl.2010.01.010.

Burkhardt C., Kleine T., Bourdon B., Palme H., Zipfel J., Friedrich J. M. and Ebel D. S. (2008) Hf-W mineral isochron for Ca,Al-rich inclusions: Age of the solar system and the timing of core formation in planetesimals. *Geochim. Cosmochim. Acta* **72**, 6177–6197. Available at: http://dx.doi.org/10.1016/j.gca.2008.10.023.

Carlson R. W., Garçon M., O'Neil J., Reimink J. and Rizo H. (2019) The nature of Earth's first crust. *Chem. Geol.* **530**, 119321. Available at: https://doi.org/10.1016/j.chemgeo.2019.119321.

Caro G. (2011) Early silicate earth differentiation. *Annu. Rev. Earth Planet. Sci.* **39**, 31–58.

Caro G., Bourdon B., Birck J-L. and Moorbath S. (2006) High-precision ^{142}Nd/^{144}Nd measurements in terrestrial rocks: Constraints on the early differentiation of the Earth's mantle. *Geochim. Cosmochim. Acta* **70**, 164-191.

Chou, C-L., 1978. Fractionation of siderophile elements in the earth's upper mantle. *Proc. 9th Lunar Planet. Sci. Conf.*, pp. 219-230

Dale C. W., Kruijer T. S. and Burton K. W. (2017) Highly siderophile element and 182W evidence for a partial late veneer in the source of 3.8 Ga rocks from Isua, Greenland. *Earth Planet. Sci. Lett.* **458**, 394–404.

Day J. M. D., Brandon, A. D. and Walker R. J. (2016) Highly siderophile elements in Earth, Mars, the Moon, and Asteroids. *Rev. Mineral. Geochem.* **81**, 161-238.

Day J. M. D., Pearson G., Taylor D. and Lawrence A. (2007) Highly siderophile element constraints on accretion and differentiation of the Earth-Moon system. *Science* **315**, 217–219.

Debaille V., O'Neill C., Brandon A. D., Haenecour P., Yin Q. Z., Mattielli N. and Treiman A. H. (2013) Stagnant-lid tectonics in early Earth revealed by Nd-142 variations in late

Archean rocks. *Earth Planet. Sci. Lett.* **373**, 83–92. Available at: http://dx.doi.org/10.1016/j.epsl.2013.04.016.

Fischer R. A. and Nimmo F. (2018) Effect of core formation on the Hf-W isotopic composition of the Earth and dating of the Moon-forming impact. *Earth Planet. Sci. Lett.* **499**, 257–265.

Fischer-Gödde M. and Becker H. (2012) Osmium isotope and highly siderophile element constraints pn ages and nature of meteoritic components in ancient lunar impact rocks. *Geochim. Cosmochim. Acta* **77**, 135-156.

Halliday A. N. and Wood B. J. (2009) How did earth accrete? *Science* **325**, 44–45.

Halliday A., Rehkämper M., Lee D-C. and Yi W. (1996) Early evolution of the Earth and Moon: new constraints from Hf-W isotope geochemistry. *Earth Planet. Sci. Lett.* **142**, 75-89.

Harper C. L. and Jacobsen S. B. (1996) Evidence for ^{182}Hf in the early Solar System and constraints on the timescale of terrestrial accretion and core formation. *Geochim. Cosmochim. Acta* **60**, 1131–1153.

Harrison T. M., Schmitt A. K., McCulloch M. T. and Lovera O. M. (2008) Early (≥ 4.5 Ga) formation of terrestrial crust: Lu-Hf, δ^{18}O, and Ti thermometry results for Hadean zircons. *Earth Planet. Sci. Lett.* **268**, 476–486.

Jacobsen S. B. and Wasserburg G. J. (1979) Nd and Sr isotopic study of the Bay of Islands ophiolite complex and the evolution of the source of mid-ocean ridge basalts. *J. Geophys. Res.* **84**, 7429–7445.

Jacobsen, S. B. and Harper, C. L., Jr. (1996) Accretion and early differentiation of the Earth based on exticnt radionuclides. In: Basu, A., Hart, S.R. (Eds.), Earth processes: reading the isotopic code. American Geophysical Union, pp. 47-74.

Jones, R. E., van Keken, P. E., Hauri, E. H., Tucker, J. M., Vervoort, J. and Ballentine, C. J. (2019) Origins of the terrestrial Hf-Nd mantle array: Evidence from a combined geodynamical-geochemical approach. *Earth Planet. Sci. Lett.* **518**, 26-39.

Kimura K., Lewis R. S. and Anders E. (1974) Distribution of gold and rhenium between nickel-iron and silicate melts: implications for the abundance of siderophile elements on the Earth and Moon. *Geochim. Cosmochim. Acta* **38**, 683–701.

Kleine T. (2011) Earth's patchy late veneer. *Nature* **477**, 168–169.

Kleine T. and Walker R. J. (2017) Tungsten Isotopes in Planets. *Annu. Rev. Earth Planet. Sci.* **45**, 389–417.

Kleine T., Mezger K., Münker C., Palme H. and Bischoff A. (2004) ^{182}Hf-^{182}W isotope systematics of chondrites, eucrites, and martian meteorites: Chronology of core formation and early mantle differentiation in Vesta and Mars. *Geochim. Cosmochim. Acta* **68**, 2935–2946.

Kleine T., Münker C., Mezger K. and Palme H. (2002) Rapid accretion and early core formation on asteroids and the terrestrial planets from Hf-W chronometry. *Nature* **418**, 952–955.

Kleine T., Touboul M., Bourdon B., Nimmo F., Mezger K., Palme H., Jacobsen S. B., Yin Q. Z. and Halliday A. N. (2009) Hf-W chronology of the accretion and early evolution of asteroids and terrestrial planets. *Geochim. Cosmochim. Acta* **73**, 5150–5188. Available at: http://dx.doi.org/10.1016/j.gca.2008.11.047.

Kring D. A. and Cohen B. A. (2002) Cataclysmic bombardment throughout the inner solar system 3.9-4.0 Ga. *J. Geophys. Res. E Planets* **107**, 5009.

Kruijer T. S. and Kleine T. (2017) Tungsten isotopes and the origin of the Moon. *Earth Planet. Sci. Lett.* **475**, 15–24. Available at: http://dx.doi.org/10.1016/j.epsl.2017.07.021.

Kruijer T. S., Kleine T., Fischer-Gödde M. and Sprung P. (2015) Lunar tungsten isotopic evidence for the late veneer. *Nature* **520**, 534–537.

Kumari S., Paul D. and Stracke A. (2016) Open system models of isotopic evolution in Earth's silicate reservoirs: Implications for crustal growth and mantle heterogeneity. *Geochim. Cosmochim. Acta* **195**, 142–157. Available at: http://dx.doi.org/10.1016/j.gca.2016.09.011.

Kumari S., Paul D. and Stracke A. (2019) Constraints on Archean crust formation from open system models of Earth evolution. *Chem. Geol.* **530**, 119307. Available at: https://doi.org/10.1016/j.chemgeo.2019.119307.

Lee D. C. and Halliday A. N. (1995) Hafnium–tungsten chronometry and the timing of terrestrial core formation. *Nature* **378**, 771–774.

Lesher C. E., Dannberg J., Barfod G. H., Bennett N. R., Glessner J. J. G., Lacks D. J. and Brenan J. M. (2020) Iron isotope fractionation at the core–mantle boundary by thermodiffusion. *Nat. Geosci.* **13**, 382–386. Available at: http://dx.doi.org/10.1038/s41561-020-0560-y.

Liu J., Touboul M., Ishikawa A. and Walker R. J. (2016) Widespread tungsten isotope anomalies and W mobility in crustal and mantle rocks of the Eoarcjean Saglek Block, northern Labrador, Canada: Implications for early Earth processes and W recycling. *Geochim. Cosmochim. Acta* **448**, 13-23.

Maas C., Manske L., Wünnemann K. and Hansen U. (2021) On the fate of impact-delivered metal in a terrestrial magma ocean. *Earth Planet. Sci. Lett.* **554**, 116680.

Maier W. D., Barnes Stephen J., Campbell I. H., Fiorentini M. L., Peltonen P., Barnes Sarah Jane and Smithies R. H. (2009) Progressive mixing of meteoritic veneer into the early Earths deep mantle. *Nature* **460**, 620–623.

Marchi S., Canup R. M. and Walker R. J. (2018) Heterogeneous delivery of silicate and metal to the Earth by large planetesimals. *Nat. Geosci.* **11**, 77-81.

Maurice M., Tosi N., Schwinger S., Breuer D. and Kleine T. (2020) A long-lived magma ocean on a young Moon. *Sci. Adv.* **6**, eaba8949.

McCoy T. J., Walker R. J., Goldstein J. I., Yang J., McDonough W. F., Rumble D., Chabot N. L., Ash R. D., Corrigan C. M., Michael J. R. and Kotula P. G. (2011) Group IVA irons: New constraint on the crystallization and cooling history of an asteroidal core with a complex history. *Geochim. Cosmochim. Acta* **75**, 6821-6843.

McDonough W. F. (2014) Compositional Model for the Earth's Core. 3rd ed., Elsevier Ltd. Available at: http://dx.doi.org/10.1016/B978-0-08-095975-7.00215-1.

Mundl A., Touboul M., Jackson M. G., Day J. M. D., Kurz M. D., Lekic V., Helz R. T. and Walker R. J. (2017) Tungsten-182 heterogeneity in modern ocean island basalts. *Science* **356**, 66–69.

Mundl A., Walker R. J., Reimink J. R., Rudnick R. M. and Gaschnig R. M. (2018) Tungsten-182 in the upper continental crust: Evidence from glacial diamictites. *Chem. Geol.* **494**, 144-152.

Mundl-Petermeier A., Walker R. J., Fischer R. A., Lekic V., Jackson M. G. and Kurz M. D. (2020) Anomalous ^{182}W in high ^{3}He/^{4}He ocean island basalts: Fingerprints of Earth's core? *Geochim. Cosmochim. Acta* **271**, 194–211. Available at: https://doi.org/10.1016/j.gca.2019.12.020.

Newsom H. E., Sims K. W. W., Noll P. D., Jaeger W. L., Maehr S. A. and Beserra T. B. (1996) The depletion of tungsten in the bulk silicate earth: Constraints on core formation. *Geochim. Cosmochim. Acta* **60**, 1155–1169.

O'Neil J., Rizo H., Boyet M., Carlson R. W. and Rosing M. T. (2016) Geochemistry and Nd isotopic characteristics of Earth's Hadean mantle and primitive crust. *Earth Planet. Sci. Lett.* **442**, 194–205. Available at: http://dx.doi.org/10.1016/j.epsl.2016.02.055.

Paul D., White W. M. and Turcotte D. L. (2002) Modelling the isotopic evolution of the Earth. *Philos. Trans. R. Soc. A Math. Phys. Eng. Sci.* **360**, 2433–2474.

Puchtel I. S., Blichert-Toft J., Touboul M. and Walker R. J. (2018) ^{182}W and HSE constraints from 2.7 Ga komatiites on the heterogeneous nature of the Archean mantle. *Geochim. Cosmochim. Acta* **228**, 1–26. Available at: https://doi.org/10.1016/j.gca.2018.02.030.

Puchtel I. S., Blichert-Toft J., Touboul M., Horan M. F. and Walker R. J. (2016) The coupled ^{182}W-^{142}Nd record of early terrestrial mantle differentiation *Geochemistry Geophys. Geosystems* **17**, 2168–2193.

Puchtel I. S., Mundlt-Petermeier, A., Horan, M., Hanski, E.J., Blichert-Toft J. and Walker R. J. (2020) Ultra-depleted 2.05 Ga komatiites of Finnish Lapland: Products of grainy late accretion or core-mantle interaction? *Chem. Geol.* **554**, 119801.

Reimink, J. R., Chacko, T., Carlson, R. W., Shirey, S. B., Liu, J., Stern, R. A., Bauer, A. M., Pearson, D. G. and Heaman, L. M. (2018). Pertogenesis and tectonics of the Acasta Gneiss complex derived from intergrated petrology and ^{142}Nd and ^{182}W extinct nuclide-geochemistry, *Earth Planet. Sci. Lett.* **494**, 12-22.

Righter K. and Shearer C. K. (2003) Magmatic fractionation of Hf and W: Constraints on the timing of core formation and differentiation in the Moon and Mars. *Geochim. Cosmochim. Acta* **67**, 2497–2507.

Rizo H., Andrault D., Bennett N. R., Humayun M., Brandon A., Vlastelic I., Moine B., Poirier A., Bouhifd M. A. and Murphy D. T. (2019) ^{182}W evidence for core-mantle interaction in the source of mantle plumes. *Geochemical Perspect. Lett.* **11**, 6–11.

Rizo H., Boyet M., Blichert-Toft J. and Rosing M. (2011) Combined Nd and Hf isotope evidence for deep-seated source of Isua lavas. *Earth Planet. Sci. Lett.* **312**, 267–279. Available at: http://dx.doi.org/10.1016/j.epsl.2011.10.014.

Rizo H., Boyet M., Blichert-Toft J. and Rosing M. T. (2013) Early mantle dynamics inferred from 142Nd variations in Archean rocks from southwest Greenland. *Earth Planet. Sci. Lett.* **377**–**378**, 324–335. Available at: http://dx.doi.org/10.1016/j.epsl.2013.07.012.

Rizo H., Walker R. J., Carlson R. W., Touboul M., Horan M. F., Puchtel I. S., Boyet M. and Rosing M. T. (2016) Early Earth differentiation investigated through ^{142}Nd, ^{182}W, and highly siderophile element abundances in samples from Isua, Greenland. *Geochim. Cosmochim. Acta* **175**, 319–336. Available at: http://dx.doi.org/10.1016/j.gca.2015.12.007.

Rosas J. C. and Korenaga J. (2018) Rapid crustal growth and efficient crustal recycling in the early Earth: Implications for Hadean and Archean geodynamics. *Earth Planet. Sci. Lett.* **494**, 42–49. Available at: https://doi.org/10.1016/j.epsl.2018.04.051.

Roth A. S. G., Bourdon B., Mojzsis S. J., Rudge J. F., Guitreau M. and Blichert-Toft J. (2014) Combined ^{147,146}Sm-^{143,142}Nd constraints on the longevity and residence time of early terrestrial crust. *Geochemistry Geophys. Geosystems* **15**, 2329–2345.

Roth A. S. G., Bourdon B., Mojzsis S. J., Touboul M., Sprung P., Guitreau M. and Blichert-Toft J. (2013) Inherited 142Nd anomalies in Eoarchean protoliths. *Earth Planet. Sci. Lett.* **361**, 50–57. Available at: http://dx.doi.org/10.1016/j.epsl.2012.11.023.

Rudge J. F., Kleine T. and Bourdon B. (2010) Broad bounds on Earth's accretion and core formation constrained by geochemical models. *Nat. Geosci.* **3**, 439–443. Available at: http://dx.doi.org/10.1038/ngeo872.

Rudnick R. L. and Gao S. (2014) Composition of the continental crust. In Treatise on Geochemistry (eds. H. D. Holland and K. K. Turekian). Elsevier, Amsterdam, pp. 1–64.

Saji N. S., Larsen K., Wielandt D., Schiller M., Costa M. M., Whitehouse M. J., Rosing M. T. and Bizzarro M. (2018) Hadean geodynamics inferred from time-varying ^{142}Nd/^{144}Nd in the early Earth rock record. *Geochemical Perspect. Lett.* **7**, 43–48.

Salters, V. J. M. and Stracke, A. (2004) Composition of the depleted mantle. *Geochem. Geophys. Geosyst.* **5**, 1–27. Available at: https://doi.org/10.1029/2003GC000597.

Taylor, S. R. (1964) Abundance of chemical elements in the continental crust: a new table. *Geochim. Cosmochim. Acta* **28**, 1273–1285.

Taylor, S. R. and McLennan, S.M. (1995) The geochemical evolution of the continental crust. *Am. Geophys. Union* **33**, 241–265.

Tera F., Papanastassiou D. A. and Wasserburg G. J. (1974) Isotopic evidence for a terminal lunar. *Earth Planet. Sci. Lett.* **22** 1-21. Available at: http://www.sciencedirect.com/science/article/pii/0012821X74900594.

Touboul M., Liu J., O'Neil J., Puchtel I. S. and Walker R. J. (2014) New insights into the Hadean mantle revealed by ^{182}W and highly siderophile element abundances of supracrustal rocks from the Nuvvuagittuq Greenstone Belt, Quebec, Canada. *Chem. Geol.* **383**, 63–75. Available at: http://dx.doi.org/10.1016/j.chemgeo.2014.05.030.

Touboul M., Puchtel I. S. and Walker R. J. (2012) ^{182}W evidence for long-term preservation of early mantle differentiation products. *Science* **335**, 1065–1069.

Touboul M., Puchtel I. S. and Walker R. J. (2015) Tungsten isotopic evidence for disproportional late accretion to the Earth and Moon. *Nature* **520**, 530–533.

Turcotte D. L., Paul D. and White W. M. (2001) Thorium-uranium systematics require layered mantle convection. *J. Geophys. Res. Solid Earth* **106**, 4265–4276.

Tusch J., Sprung, P., Löcht van de, Hofmann J. E., Boyd A. J., Rosing M. T., Münker C. (2019) Uniform ^{182}W isotope compositions in Eoarchean rocks from the Isua region, SW Greenland: The role of early silicate differentiation and missing late veneer. *Geochim. Cosmochim. Acta* **257**, 248-310.

van de Löcht J., Hoffmann J. E., Li C., Wang Z., Becker H., Rosing M. T., Kleinschrodt R. and Münker C. (2018) Earth's oldest mantle peridotites show entire record of late accretion. *Geology* **46**, 199–202.

Wade J. and Wood B. J. (2005) Core formation and the oxidation state of the Earth. *Earth Planet. Sci. Lett.* **236**, 78–95.

Walker R. J. (2009) Highly siderophile elements in the Earth, Moon and Mars: Update and implications for planetary accretion and differentiation. *Chemie der Erde* **69**, 101–125.

Walker R. J., McDonough W. F., Honesto J., Chabot N. L., McCoy T., Ash R. D. and Bellucci J. J. (2008) Modeling fractional crystallization of group IVB iron meteorites. *Geochim. Cosmochim. Acta* **72**, 2198–2216.

Wilde S. A., Valley J. W., Peck W. H. and Graham C. M. (2001) Evidence from detrital zircons for the existence of continental crust. *Nature* **409**, 175–178.

Willbold M., Elliott T. and Moorbath S. (2011) The tungsten isotopic composition of the Earthgs mantle before the terminal bombardment. *Nature* **477**, 195–198. Available at: http://dx.doi.org/10.1038/nature10399.

Willbold M., Mojzsis S. J., Chen H. W. and Elliott T. (2015) Tungsten isotope composition of the Acasta Gneiss Complex. *Earth Planet. Sci. Lett.* **419**, 168–177. Available at: http://dx.doi.org/10.1016/j.epsl.2015.02.040.

Workman, R. K. and Hart, S. R. (2005) Major and trace element composition of the depleted MORB mantle (DMM). *Earth Planet. Sci. Lett.* **231**, 53–72. Available at: https://doi.org/10.1016/j.epsl.2004.12.005.

Yin Q., Jacobsen S. B., Yamashita K., Blichert-Toft J., Télouk P. and Albarède F. (2002) A short timescale for terrestrial planet formation from Hf-W chronometry of meteorites. *Nature* **418**, 949–952.

FIGURE CAPTIONS

Fig. 1. Schematic representation of a five-reservoir open-system model of the Earth showing the mass fluxes between the reservoirs. The core and the silicate reservoirs exchange material only during core formation. Subsequently, late accreted material is added to the mantle reservoirs with concurrent silicate differentiation, that is, formation of continental crust and its recycling into the mantle.

Fig. 2. The calculated radiogenic contribution of ^{182W} from ^{182}Hf decay in a BSE-like reservoir, calculated by $(^{182}Hf/^{180}Hf)t_{CF}$ x $(^{180}Hf/^{184}W)_{BSE}$; t_{CF} is the time after solar system initial (4.56 Ga) when core formation ended, and thus the starting point of the BSE evolution. For a BSE-like reservoir with $(^{180}Hf/^{184}W)_{BSE}$ = 25.4 (Kleine and Walker, 2017), the radiogenic contribution of ^{182}W from ^{182}Hf decay is analytically resolvable (i.e., >5 ppm) for core formation periods up to ~80 Myr, for $(^{182}Hf/^{180}Hf)t_{CF}$ starting from a solar system initial $(^{182}Hf/^{180}Hf)i = 1.018 \times 10^{-4}$.

Fig. 3. Diagrams showing (a) three different core growth models for a total duration t_{CF} = 45 Myr, and (b) the corresponding evolution of $\mu^{182}W_{BSE}$ with (dashed lines) and without (solid lines) adding late accreted material (LAM) to achieve a present-day $\mu^{182}W_{BSE}$ = 0. The black lines are for linear growth, the red curves show results for 90% of core growth within the first 10 Myr and the blue curve for 90% of core growth within the last 10 Myr of the entire 45 Myr core formation period. Also listed in panel (b) is the mass of LAM (relative to bulk Earth mass) and the $\mu^{182}W_{BSE}$ and W concentration ($^{182}W_{BSE}$) at the end of core formation (45 Myr) for each of the three scenarios. Similar plots for core formation periods of 30, 60, and 100 Myr are provided in the supplementary materials (Fig. S1, S2, and S3). These results for each model are also listed in Table 4.

Fig. 4. Modeled $\mu^{182}W_{BSE}$ evolution with (green lines) and without late accretion (black lines) for four different core formation times ($_{t}CF$) of 30, 45, 60, and 100 Myr after solar system formation at 4.56 Ga. The green lines show the isotopic evolution of $\mu^{182}W_{BSE}$ after core formation to $\mu^{182}W_{BSE}$ = 0 at 4.41 Ga by the addition of late accreted material of bulk Earth-like composition; the amount of late accreted material (LAM) for each t_{CF} is given in wt% of the bulk Earth mass. The end of late accretion at 4.41 Ga is chosen for illustrative purposes, i.e., to clearly resolve the differences between the individual model curves.

Fig. 5. The diagram shows the amount of late accreted material (LAM) versus the W concentration in the bulk silicate earth (W_{BSE}) for different core formation periods (t_{CF}) and rates of core formation. Different colors represent variable core formation periods and different symbols represents variable core formation rates. The squares represents models where 90% of the core forms in the initial 10 Myr, the circle represents linear core formation models, and the triangle represents models where 90% of the core forms in the last 10 Myr of the core formation period. Results for t_{CF} = 100 Myr also include cases where 70% and 50% of the core formed by the initial 30 Myr, shown here with the + symbol. Data are from Table 4 and Table S5. Present-day W_{BSE} = 13 ± 10 (2SD) is shown by the shaded gray box.

Fig. 6. (a) Plots showing three different late accretion scenarios in which same amount of late accreted material (LAM) is added to the mantle after core formation. Core formation ends at 45 Myr after solar system formation and late accretion ends at 3.8 Ga. The rate of accretion is varied by adding either 90% of total late accreted material to the mantle in the initial 100 Myr of total late accretion time period (rapid late accretion (LA) scenario) or 90% of total late accreted material to the mantle in the last 100 Myr of total late accretion time period (delayed late accretion scenario). Linear late accretion assumes a constant flux of late accreted material to the mantle in each time interval of late accretion. Panel (b) shows the modeled evolution of

$\mu^{182}W_{BSE}$ for the three different late accretion scenarios, panel (c) the evolution of $\mu^{182}W$ for the modeled UM reservoir, and panel (d) the $\mu^{182}W$ evolution curves for all modeled reservoirs combined. The pink box shows the target range for $\mu^{182}W_{UM}$ = +10 to +15 between 4.0 and 2.5 Ga.

Fig. 7. Plots showing the temporal evolution of $\mu^{182}W$ in all the silicate reservoirs with concurrent silicate differentiation and late accretion. Late accretion (LA) to the mantle starts directly after core formation at (a) 30, (b) 45, (c) 60, and (d) 100 Ma and proceeds until 3.8 Ga. Also shown are isotopic evolution curves for variable recycling fluxes to the UM, adjusted by the model parameter f_R, which is the fraction of recycled crust (CC) going to the UM (f_R = 0.1 to 0.9). The remainder of the crustal recycling flux ($1 - f_R$) is stored in the IR reservoir for 1 Gyr before being mixed with the LM. The present-day $\mu^{182}W$ of the terrestrial standard is 0 ± 3.9 (2SD), shown as a green box. The heading in each panel, e.g., "t_{CF}_45Myr_LA_760Myr_f_R(0.1, 0.4, 0.9)_IT_1000Myr" lists the model parameters used in each simulation. For example, t_{CF}_45Myr, means a 'core formation time' of 45 Ma after Earth formation, LA_760Myr refers to a total 'late accretion' period of 760 Myr after Earth formation, f_R is the fraction of the recycling flux from the CC into the UM, and IT_1000Myr indicates that the recycled CC material that goes into the IR ($1- f_R$) is stored in the IR for 1000 Myr before being mixed to the LM. The same notation is used in the headings of all subsequent figures and summarizes the key model parameters of each simulation. More detailed model parameters are given in Supplementary Tables S1 and S2.

Fig. 8. Diagram showing the temporal evolution of $\mu^{182}W$ in all the silicate reservoirs for concurrent silicate differentiation and late accretion (LA) after a core formation period of 45 Myr. Here, late accreted material is added non-uniformly to the mantle for a total period of 760 Myr after solar system initial with 2% being added to the UM and the remaining 98% to the LM. The $\mu^{182}W_{UM}$ evolution successfully reproduces the observed excess 182W (10–15 ppm) reported in Hadean-Archean rocks, which is shown by the pink shaded region. The kink in the $\mu^{182}W_{UM}$ evolution observed immediately after the end of late accretion at 3.8 Ga marks the effect of crustal recycling, which becomes more pronounced after the end of late accretion at 3.8 Ga and protracts the time interval of $\mu^{182}W_{UM}$ ~+10–15 until the end of Archean. The effect of variable isolation times (IT: 10, 1000, and 5000 Myr) of recycled material in the IR on the evolution of $\mu^{182}W$ in all the reservoirs is also shown. For further details of the model see main text and Table S3 (t_{CF} = 45 Myr). The present-day $\mu^{182}W_{BSE}$ = 0 ± 3.9 (2SD) is shown by the green box. Results for core formation periods of 30, 60 and 100 Myr are shown in Fig. S4.

Fig. 9. Diagrams showing the $\mu^{182}W$ evolution in all modeled silicate reservoirs for a core formation time t_{CF} = 45 Myr with non-uniform mixing of late accreted material (LA) to the mantle until 760 Myr after Earth formation (3.8Ga). Comparison of isotopic evolutions for (a) addition of 2-10% of late accreted material to the UM and the remaining 90-98% to the LM using a W silicate-silicate transfer factor D_W of 200. Panel (b) shows results for addition of 2% of late accreted material to the UM and 98% to the LM, but using a higher a D_W of 300-400. The D_W = 400 case represents the successful solution also shown in Fig. 8.

Fig. 10. (a) $\mu^{142}Nd$ evolution in silicate reservoirs for silicate differentiation (and simultaneous addition of late accreted material for 760 Myr) starting after core formation time (t_{CF}) of 45 Myr; results for other core formation periods are shown in Fig. S8. Model parameters are as in Fig. 8. The green shaded region represents the present-day terrestrial average $\mu^{142}Nd$ = 0 **±** 5.6 (Rizo et al., 2013). (b) Temporal evolution of $\mu^{142}Nd$ in silicate reservoirs for t_{CF} = 45 Myr and a variable m_{UM} in the range 0.6–0.4. All other model parameters and conditions are the same as in (a). (c) Temporal evolution of $\mu^{142}Nd$ in silicate reservoirs for t_{CF} = 45 Myr and m_{UM} =

0.5. Solid lines represent μ^{142}Nd evolution with D_{Sm} and D_{Nd} used by Kumari et al. (2016, 2019), which are also used in modeling the results shown in (a) and (b). Dashed lines show isotopic evolution with higher D_{Sm} and D_{Nd} (Table 3 case II). Corresponding temporal evolution of ε^{143}Nd for cases (b) and (c) are shown in Fig. S9.

Fig. 11. Diagram showing the effect of variable core formation periods (t_{CF}) and rates of core formation (early, linear or late, as given by the labels for each curve) on $(Hf/W)_{BSE}$. Gray bar shows the range of Hf/W_{BSE} (17± 5, Kleine et al., 2009). Data are from Table 4 and Table S5.

Fig. 12. Diagram of $\mu^{182}W_{BSE}$ versus W_{BSE} showing that the pre-late accretion $\mu^{182}W_{BSE}$ at t_{CF} can be very variable and compatible with similar W_{BSE} and thus amounts of late accreted material (LAM = 0.82–1.1% in the examples shown above). Data are from Table 4 (for core formation periods of 30 and 45 Myr cases) and Table S5 (for core formation period of 100 Myr case). Note that the present-day pre-late accretion $\mu^{182}W_{BSE}$ is +25 in each case.

Fig. 13. μ^{182}W evolution in all the silicate reservoirs considering late accretion and simultaneous silicate differentiation (same way as described in Fig. 8) after core formation ends at 45 Myr, for m_{UM} of 0.6 (solid lines) and 0.5 (dashed lines). The kink in the $\mu^{182}W_{UM}$ evolution observed immediately after the end of late accretion at 3.8 Ga marks the effect of crustal recycling, which becomes more pronounced after the end of late accretion and protracts the time interval of $\mu^{182}W_{UM}$ ~+10–15 until the end of Archean. Additional model parameters and simulation conditions are provided in Table S3. Similar plots for core formation period of 30, 60, and 100 Myr are provided in Fig. S10.

Table 1. Present-day concentrations (ppm) in bulk Earth as well as the solar system initial (SSI) and present-day terrestrial standard isotopic ratios used in the model.

Concentrations (ppm)	**Bulk Earth**	**References**
Hf	0.197	McDonough (2014)
W	0.180	"
Sm	0.27	"
Nd	0.84	"
SSI	**Value**	
$^{182}W/^{184}W$	0.864598	Calculated using terrestrial standard and $\mu^{182}W_{SSI}$ of -349 ± 0.07 (Kleine and Walker, 2017)
$^{182}Hf/^{180}Hf$	$(1.018 \pm 0.043) \times 10^{-4}$	Kleine and Walker (2017); Burkhardt et al. (2008)
$^{142}Nd/^{144}Nd$	1.141462	Calculated using the modified ^{142}Nd decay equation; see eqn (1) in section 2.2
$^{146}Sm/^{144}Sm$	0.0085 ± 0.0007	Boyet et al. (2010)
Terrestrial Standard	**Value**	
$^{142}Nd/^{144}Nd$	1.141836	Roth et al. (2014)
$^{182}W/^{184}W$	0.864900	Kleine and Walker (2017)

Table 2. Model-derived present-day concentration of W (ppb) and μ^{182}W of core and silicate reservoirs for various core formation period (t_{CF}) of 30, 45, 60, and 100 Myr. Model parameters are given in Supplementary Table S3.

	Core	**BSE**	**LM**	**IR**	**UM**	**CC**	**mantle^{+}**
Target W (ppb)	**500±120**[1]	**13±10**[1]				**1000**[2]	**8.3±7.1**[1]
t_{CF} = 30 Myr							
W (ppb)	483	42.1	57.5	3010	2.04	2900	24.2
μ^{182}W	-235	-0.1	-2.6	5.2	4.0	2.9	
t_{CF} = 45 Myr							
W (ppb)	521	22.9	31.5	1640	1.1	1580	13.3
μ^{182}W	-216	0.2	-2.2	5.4	4.2	3.1	
t_{CF} = 60 Myr							
W (ppb)	543	11.8	12.2	940	0.53	750	5.2
μ^{182}W	-207	0.7	-1.7	5.8	4.7	3.6	
t_{CF} = 100 Myr							
W (ppb)	562	1.7	2.3	120	0.08	120	1.0
μ^{182}W	-199	0.03	-2.4	5.2	4.1	2.9	

Note: [1]Arevalo and McDonough (2008) and McDonough (2014) with 2σ uncertainty; [2]Rudnick and Gao (2014); $^{+}$ represents value for mean modern mantle, calculated as (W_{LM}×0.4 + W_{UM}×0.6).

Table 3

Table 3. Model-derived present-day Sm and Nd concentrations (ppm) and isotopic ratios (μ^{142}Nd and ε^{143}Nd) in UM and CC for m_{UM} = 0.50. Case I is for D_{Sm} and D_{Nd} adopted from Kumari et al. (2016, 2019) and Case II is for higher D_{Sm} and D_{Nd}.

	Target range	Case I	Case II
$D_{Sm,\ UM\rightarrow CC}$		8	12
$D_{Sm,\ LM\rightarrow CC}$		25	25
$D_{Nd,\ UM\rightarrow CC}$		18	30
$D_{Nd,\ LM\rightarrow CC}$		35	50
$C_{Sm,CC}$	3.5–6[a]	3.4	4.5
$C_{Sm,UM}$	0.58–0.71[b]	0.3	0.3
$C_{Nd,CC}$	16–28[a]	19.6	28.1
$C_{Nd,UM}$	0.24–0.27[b]	0.9	0.8
ε^{143}Nd in CC	-10 to -25[c]	-22.5	-22.9
ε^{143}Nd UM	8 to 12[c]	9.2	16.4
μ^{142}Nd in CC	-5.6 to +5.6[d]	-1.5	-0.9
μ^{142}Nd in UM	-5.6 to +5.6[d]	1.2	1.7
μ^{142}Nd in UM (@ 4.0 Ga)	~11–17.5[d]	~5.6	~10.6

Note: [a]Rudnick and Gao (2014), Taylor and McLennan (1995), Taylor (1964); [b]Workman and Hart (2005), Salters and Stracke (2004); [c]Jacobsen and Wasserburg (1979); [d]Rizo et al. (2013).

Table 4

Table 4. Model-derived result in the core and BSE, after complete core formation assuming three types of core growth, and with or without late accretion (LA) for core formation period (t_{CF}) of 30, 45, 60, and 100 Myr.

	Core formation model, t_{CF} = 30 Myr						**Core formation model, t_{CF} = 45 Myr**					
	90% in first 10 Myr		Linear		90% in last 10 Myr		90% in first 10 Myr		Linear		90% in last 10 Myr	
	no LAM at t_{CF} = 30	with LAM at t = 0	no LAM at t_{CF} = 30	with LAM at t = 0	no LAM at t_{CF} = 30	with LAM at t = 0	no LAM at t_{CF} = 45	with LAM at t = 0	no LAM at t_{CF} = 45	with LAM at t = 0	no LAM at t_{CF} = 45	with LAM at t = 0
$D_{W,silicate\text{-}metal}$	3.40		5.05		6.54		3.45		6.67		9.55	
μ^{182}_{WCore}	-281	-281	-235	-235	-217	-217	-279	-279	-216	-216	-203	-203
μ^{182W}_{BSE}	-28.0	0.50	-75.3	-0.10	-152	-0.50	7.97	0.06	-32.9	0.50	-148	0.04
W_{Core} (ppb)	410	410	483	483	519	519	413	413	521	521	551	551
W_{BSE} (ppb)	72	77	38	42	22	24	70	76	21	23	6.9	7.7
Hf/W_{BSE}	3.8	3.6	7.1	6.5	13	11	3.9	3.6	13	12	39	35
LAM		3.5%		1.9%		1.1%		3.4%		1.0%		0.34%

	Core formation model, t_{CF} = 60 Myr						**Core formation model, t_{CF} = 100 Myr**					
	90% in first 10 Myr		Linear		90% in last 10 Myr		90% in first 10 Myr		Linear		90% in last 10 Myr	
	no LAM at t_{CF} = 60	with LAM at t = 0	no LAM at t_{CF} = 60	with LAM at t = 0	no LAM at t_{CF} = 60	with LAM at t = 0	no LAM at t_{CF} = 100	with LAM at t = 0	no LAM at t_{CF} = 100	with LAM at t = 0	no LAM at t_{CF} = 100	with LAM at t = 0
$D_{W,silicate\text{-}metal}$	3.49		8.43		12.66		3.52		13.54		20.99	
μ^{182}_{WCore}	-277	-277	-207	-207	-199	-199	-276	-276	-199	-199	-197	-197
μ^{182W}_{BSE}	20.4	0.44	-9.92	-0.01	-152	0.73	24.8	-0.61	14.0	-0.04	-162	-0.01
W_{Core} (ppb)	416	416	543	543	561	561	417	417	562	562	565	565
W_{BSE} (ppb)	69	75	11	12	2.1	2.4	68	74	1.5	1.7	0.09	0.10
Hf/W_{BSE}	3.9	3.7	26	23	130	113	4.0	3.7	181	161	3048	2747
LAM		3.4%		0.52%		0.10%		3.4%		0.07%		0.004%

Figure 1

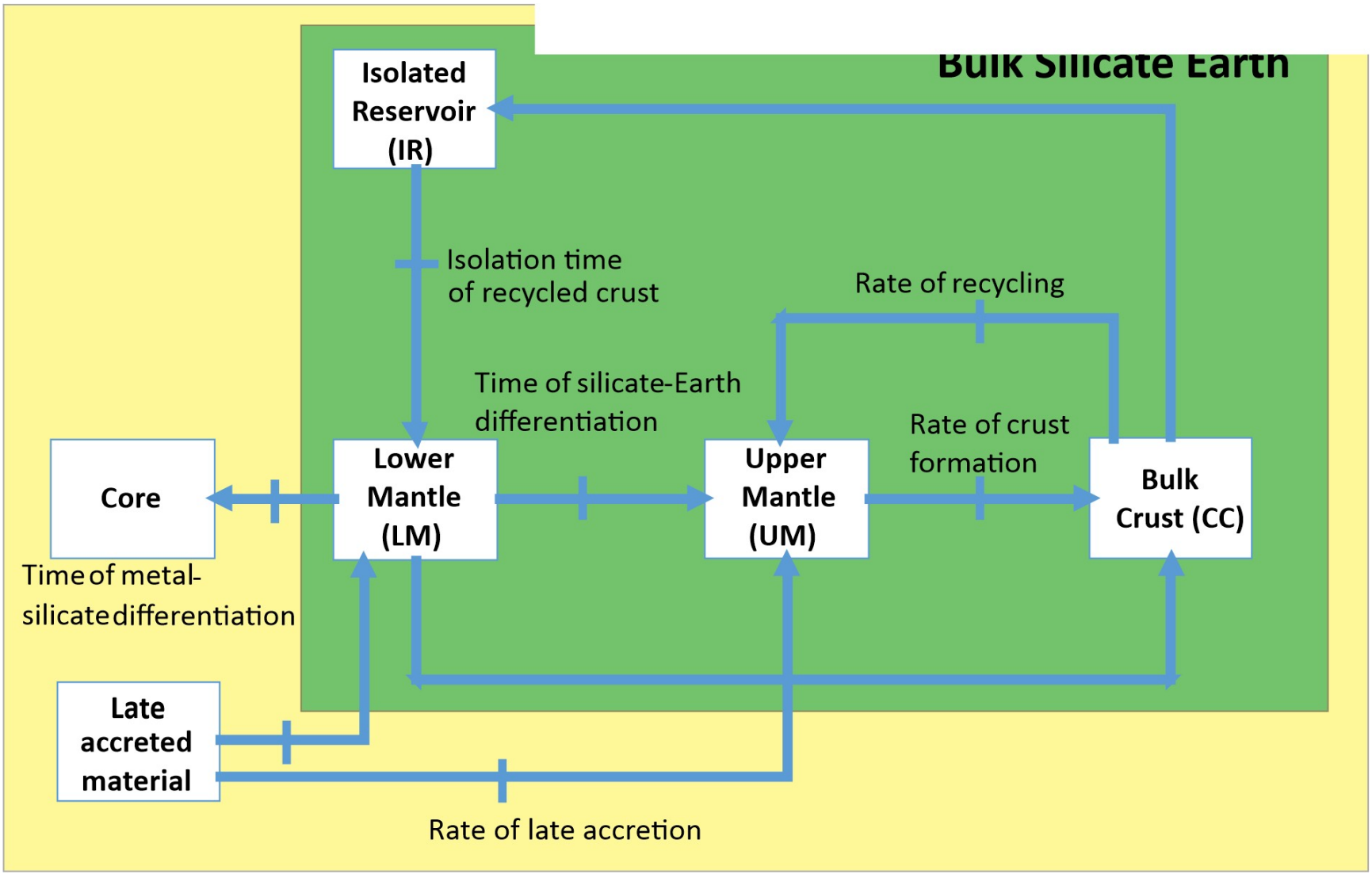
Bulk Silicate Earth
Isolated Reservoir (IR)
Isolation time of recycled crust
Rate of recycling
Time of silicate-Earth differentiation
Rate of crust formation
Core
Lower Mantle (LM)
Upper Mantle (UM)
Bulk Crust (CC)
Time of metal-silicate differentiation
Late accreted material
Rate of late accretion

Figure 2

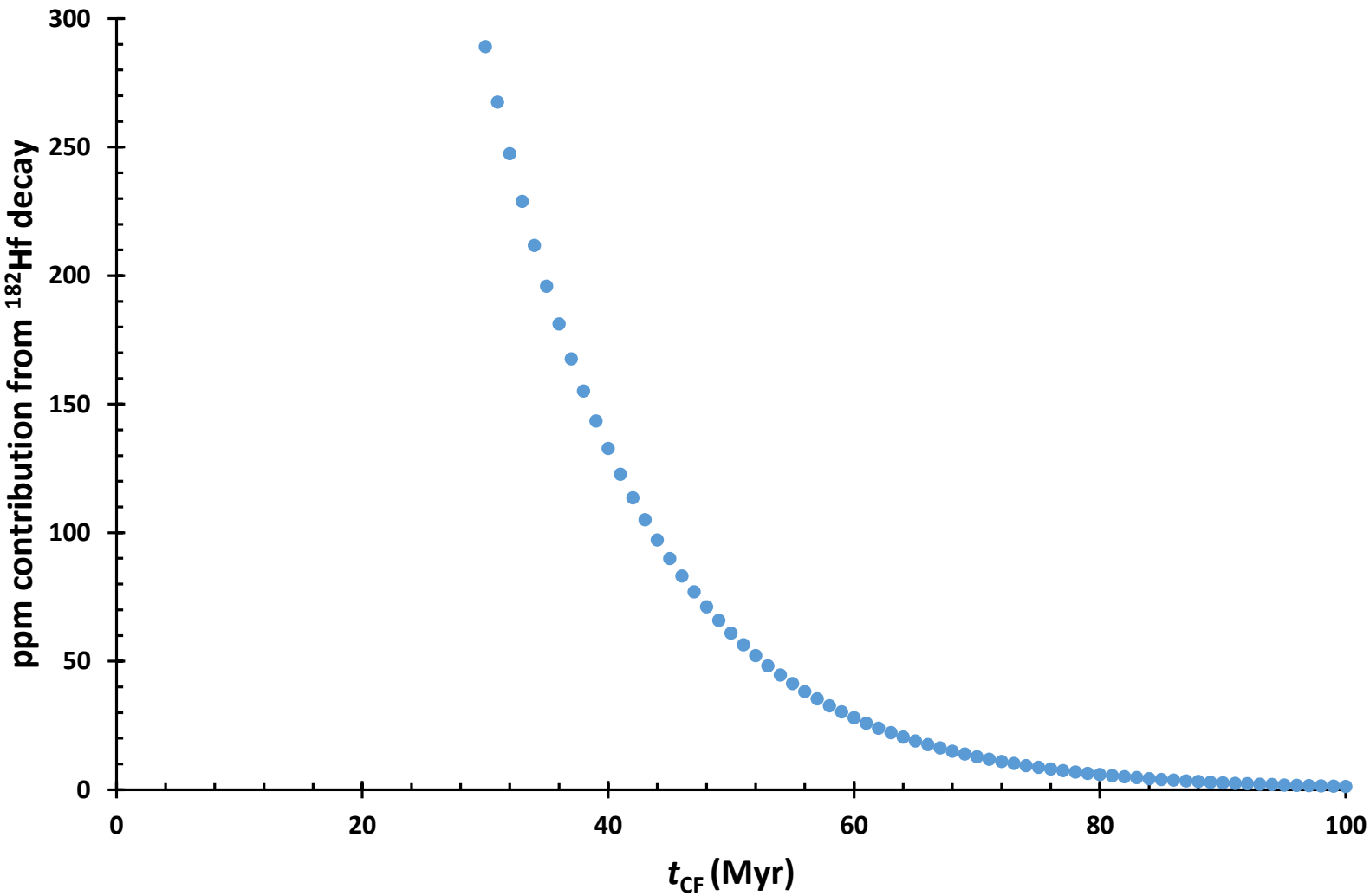
300
250
200
150
100
50
0
ppm contribution from ^{182}Hf decay
0
20
40
60
80
100
t_{CF} (Myr)

Figure 3

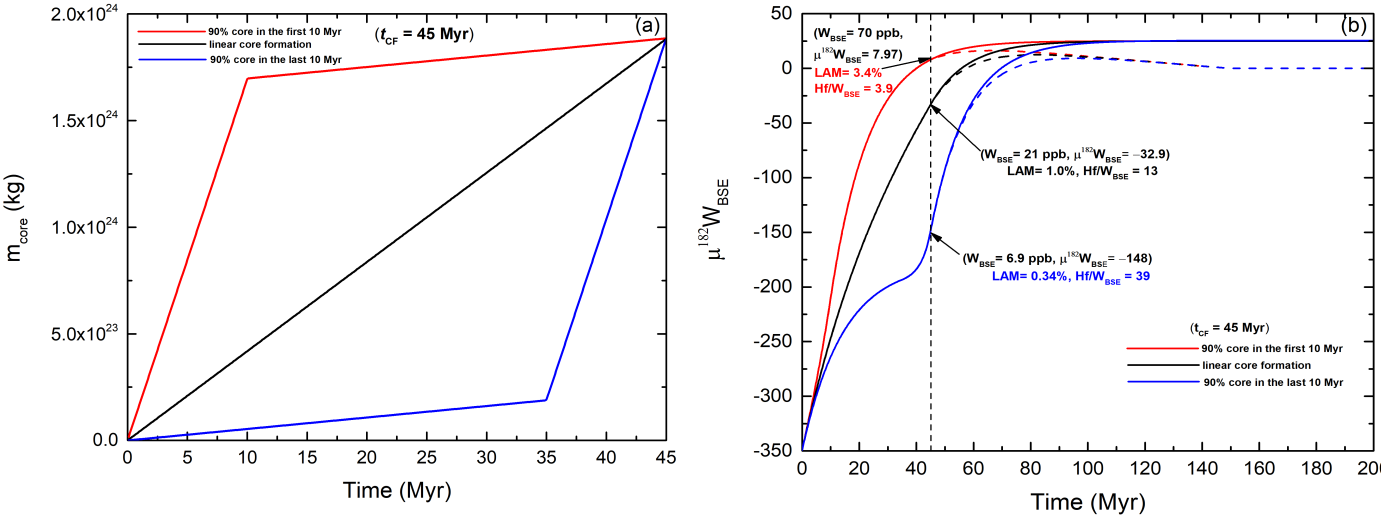
(a)
(t_{CF} = 45 Myr)
90% core in the first 10 Myr
linear core formation
90% core in the last 10 Myr
m_{core} (kg)
Time (Myr)
(b)
(W_{BSE}= 70 ppb, $\mu^{182}W_{BSE}$= 7.97)
LAM= 3.4%
Hf/W_{BSE} = 3.9
(W_{BSE}= 21 ppb, $\mu^{182}W_{BSE}$= −32.9)
LAM= 1.0%, Hf/W_{BSE} = 13
(W_{BSE}= 6.9 ppb, $\mu^{182}W_{BSE}$= −148)
LAM= 0.34%, Hf/W_{BSE} = 39
(t_{CF} = 45 Myr)
90% core in the first 10 Myr
linear core formation
90% core in the last 10 Myr
$\mu^{182}W_{BSE}$
Time (Myr)

Figure 4

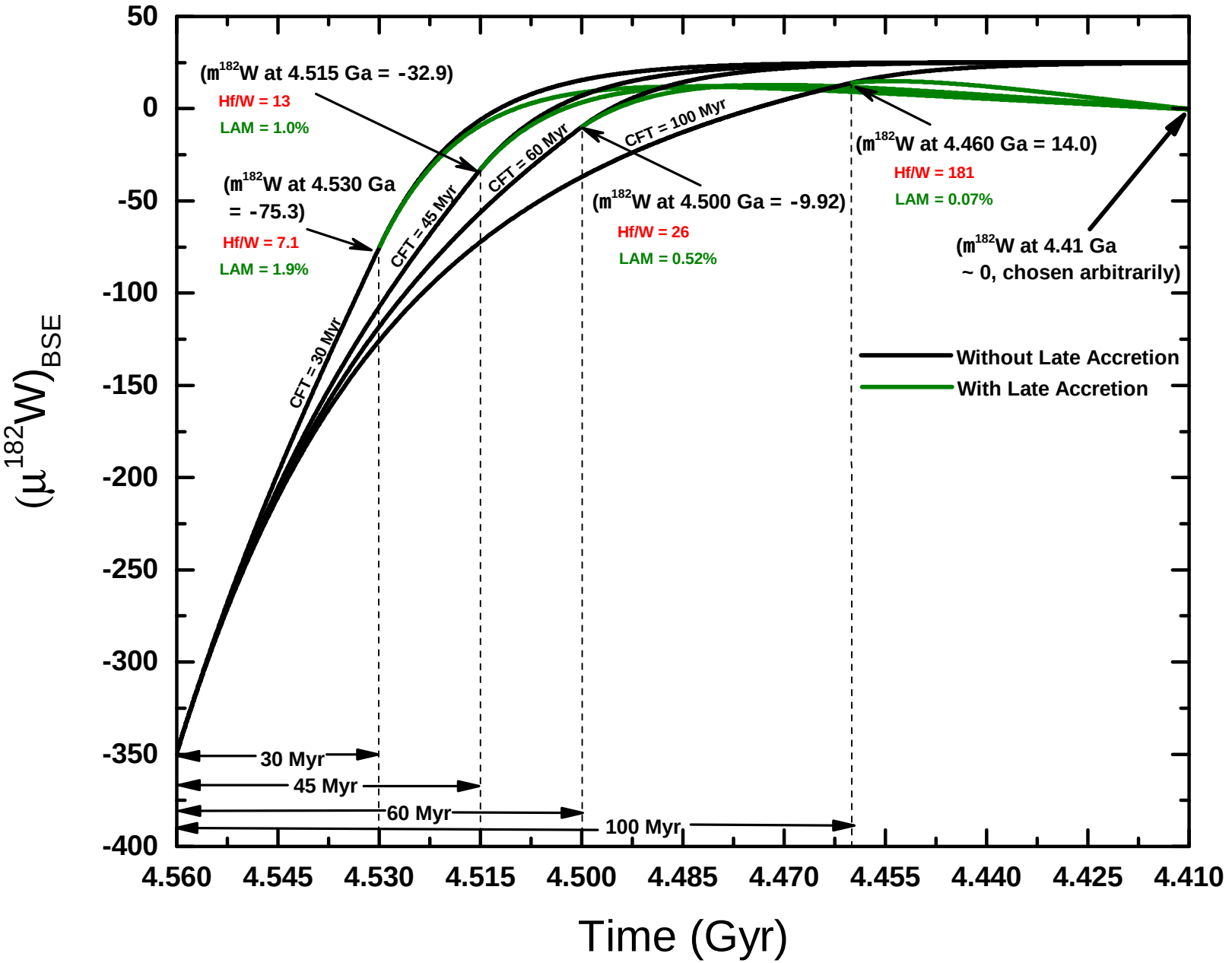
50
0
-50
-100
-150
-200
-250
-300
-350
-400
4.560
4.545
4.530
4.515
4.500
4.485
4.470
4.455
4.440
4.425
4.410
Time (Gyr)
$(\mu^{182}W)_{BSE}$
(m^{182}W at 4.515 Ga = -32.9)
Hf/W = 13
LAM = 1.0%
(m^{182}W at 4.530 Ga = -75.3)
Hf/W = 7.1
LAM = 1.9%
(m^{182}W at 4.500 Ga = -9.92)
Hf/W = 26
LAM = 0.52%
(m^{182}W at 4.460 Ga = 14.0)
Hf/W = 181
LAM = 0.07%
(m^{182}W at 4.41 Ga ~ 0, chosen arbitrarily)
CFT = 30 Myr
CFT = 45 Myr
CFT = 60 Myr
CFT = 100 Myr
30 Myr
45 Myr
60 Myr
100 Myr
Without Late Accretion
With Late Accretion

Figure 5

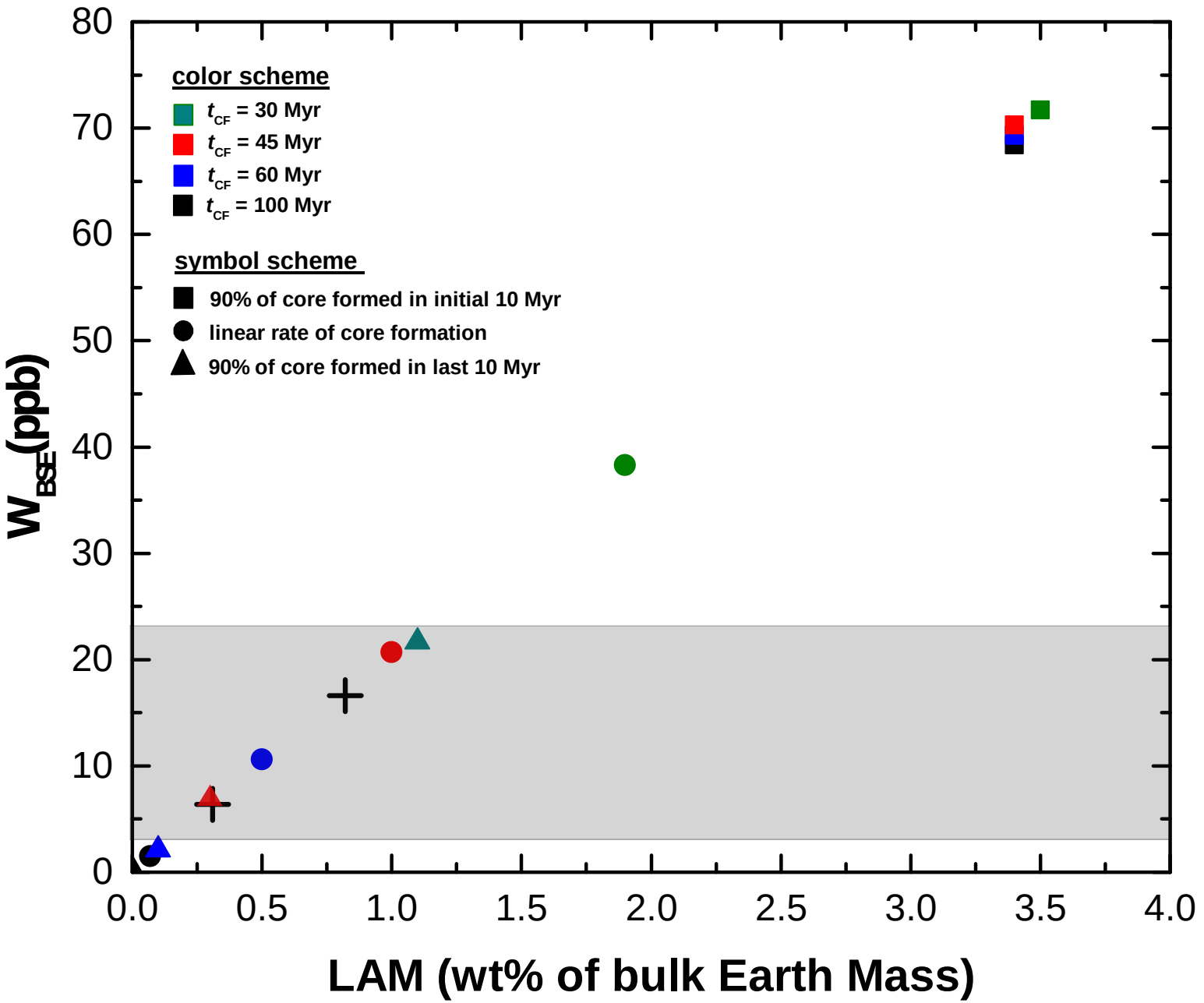
color scheme
t_{CF} = 30 Myr
t_{CF} = 45 Myr
t_{CF} = 60 Myr
t_{CF} = 100 Myr
symbol scheme
90% of core formed in initial 10 Myr
linear rate of core formation
90% of core formed in last 10 Myr
W_{BSE} (ppb)
LAM (wt% of bulk Earth Mass)
0
10
20
30
40
50
60
70
80
0.0
0.5
1.0
1.5
2.0
2.5
3.0
3.5
4.0

Figure 6

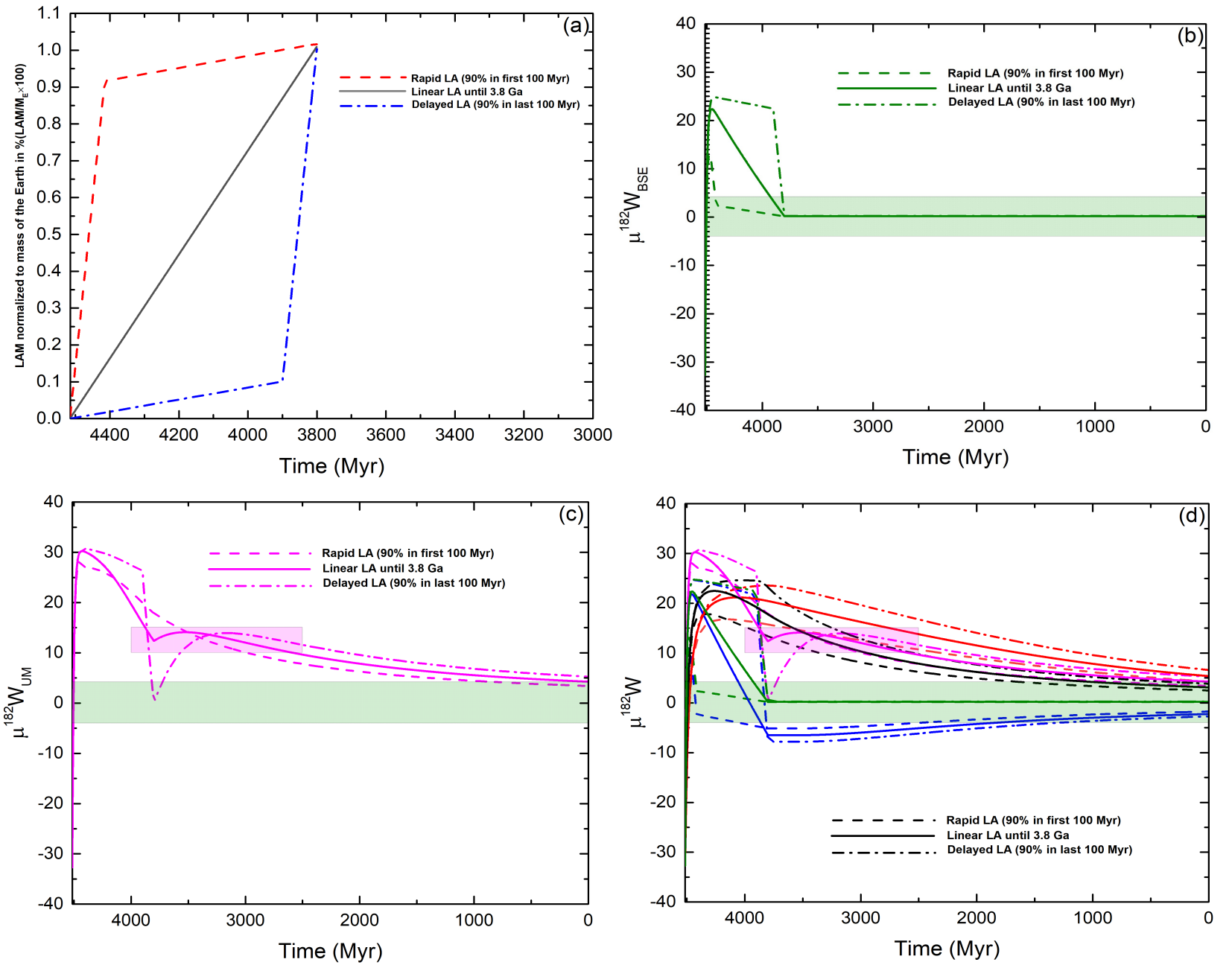
(a)
LAM normalized to mass of the Earth in %(LAM/M$_E$×100)
Time (Myr)
Rapid LA (90% in first 100 Myr)
Linear LA until 3.8 Ga
Delayed LA (90% in last 100 Myr)
(b)
$\mu^{182}W_{BSE}$
Time (Myr)
Rapid LA (90% in first 100 Myr)
Linear LA until 3.8 Ga
Delayed LA (90% in last 100 Myr)
(c)
$\mu^{182}W_{UM}$
Time (Myr)
Rapid LA (90% in first 100 Myr)
Linear LA until 3.8 Ga
Delayed LA (90% in last 100 Myr)
(d)
$\mu^{182}W$
Time (Myr)
Rapid LA (90% in first 100 Myr)
Linear LA until 3.8 Ga
Delayed LA (90% in last 100 Myr)

Figure 7

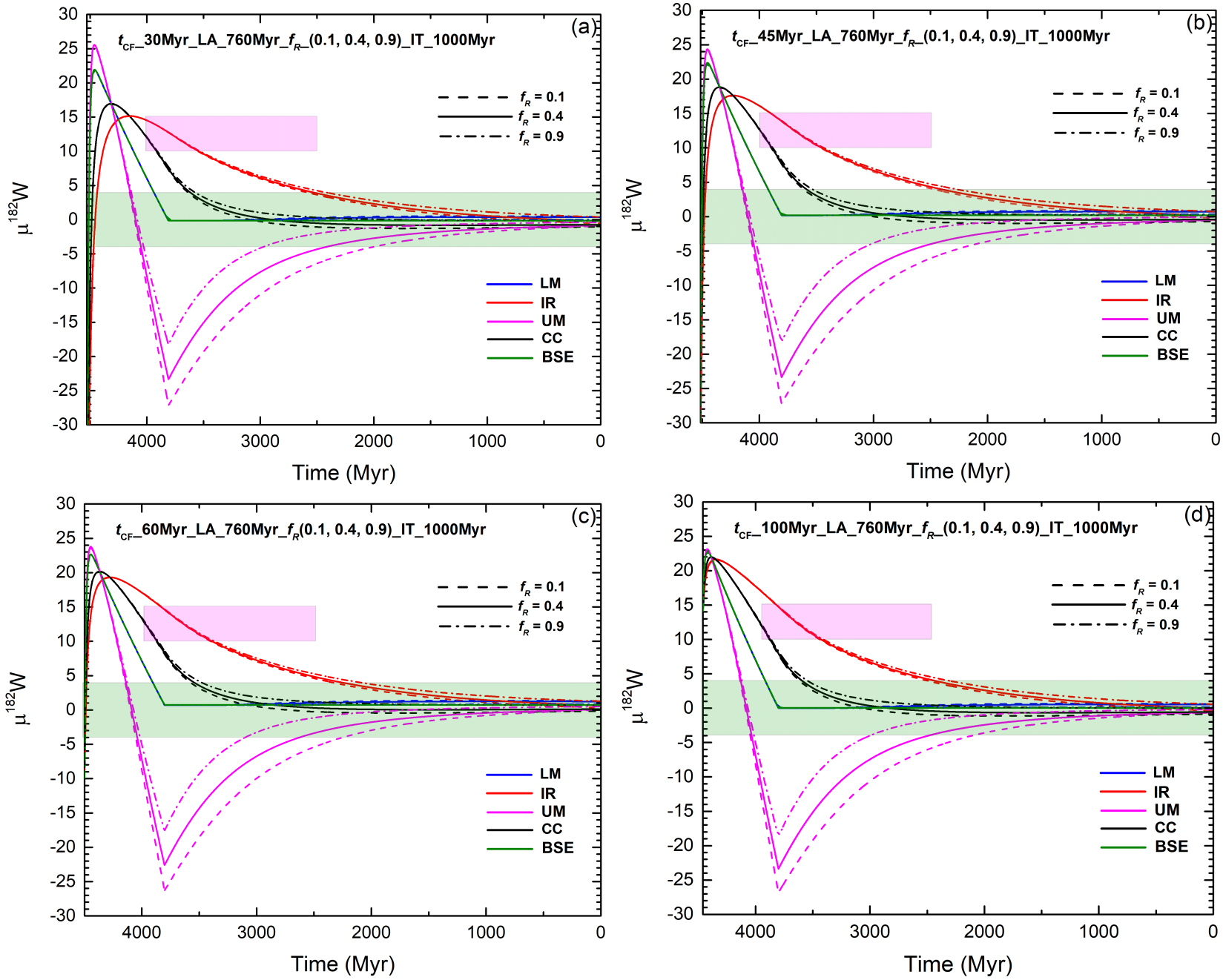
(a)
t_{CF}_30Myr_LA_760Myr_f_R_(0.1, 0.4, 0.9)_IT_1000Myr
(b)
t_{CF}_45Myr_LA_760Myr_f_R_(0.1, 0.4, 0.9)_IT_1000Myr
(c)
t_{CF}_60Myr_LA_760Myr_f_R(0.1, 0.4, 0.9)_IT_1000Myr
(d)
t_{CF}_100Myr_LA_760Myr_f_R_(0.1, 0.4, 0.9)_IT_1000Myr
f_R = 0.1
f_R = 0.4
f_R = 0.9
LM
IR
UM
CC
BSE
μ^{182}W
Time (Myr)

Figure 8

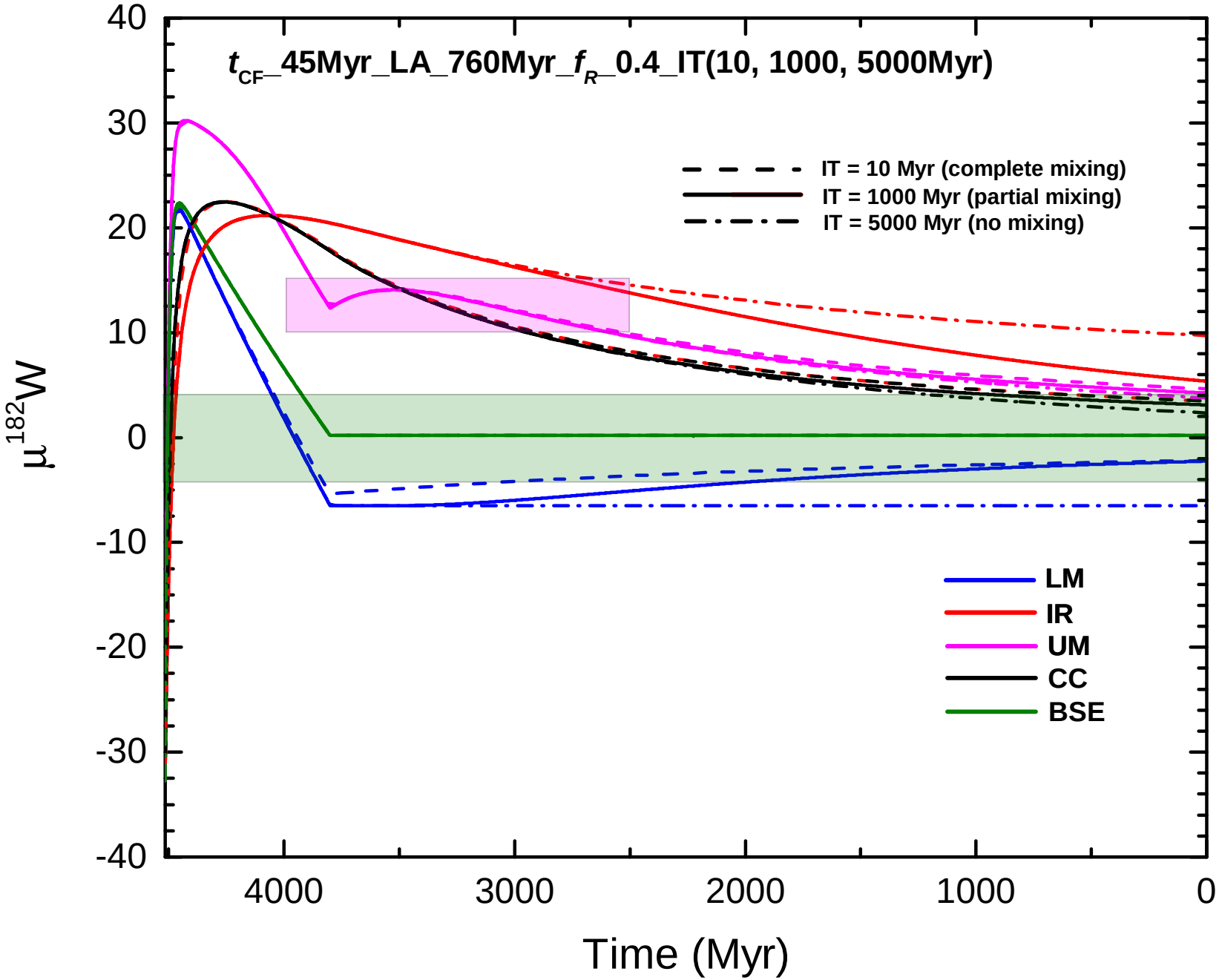
t_{CF}_45Myr_LA_760Myr_f_R_0.4_IT(10, 1000, 5000Myr)
IT = 10 Myr (complete mixing)
IT = 1000 Myr (partial mixing)
IT = 5000 Myr (no mixing)
LM
IR
UM
CC
BSE
μ^{182}W
Time (Myr)
40
30
20
10
0
-10
-20
-30
-40
4000
3000
2000
1000
0

Figure 9

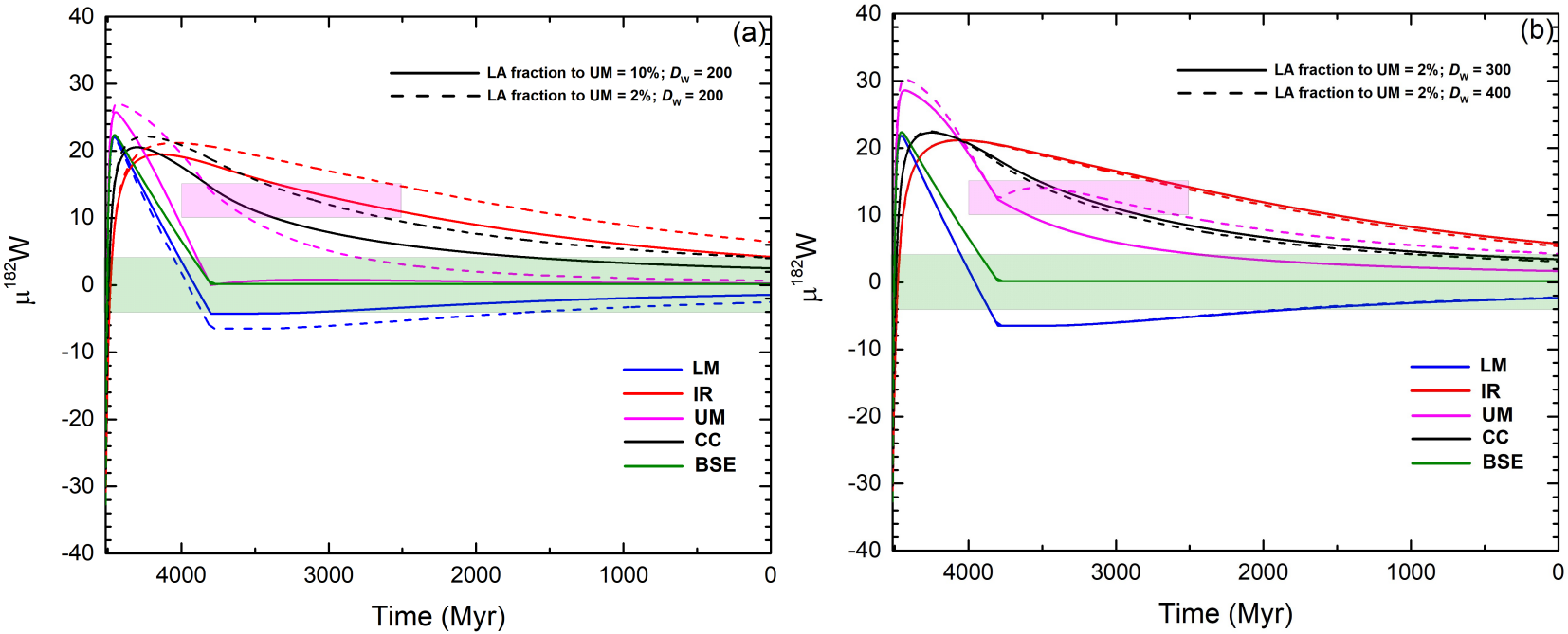
(a)
LA fraction to UM = 10%; D_w = 200
LA fraction to UM = 2%; D_w = 200
LM
IR
UM
CC
BSE
μ^{182}W
Time (Myr)
(b)
LA fraction to UM = 2%; D_w = 300
LA fraction to UM = 2%; D_w = 400
LM
IR
UM
CC
BSE
μ^{182}W
Time (Myr)

Figure 10

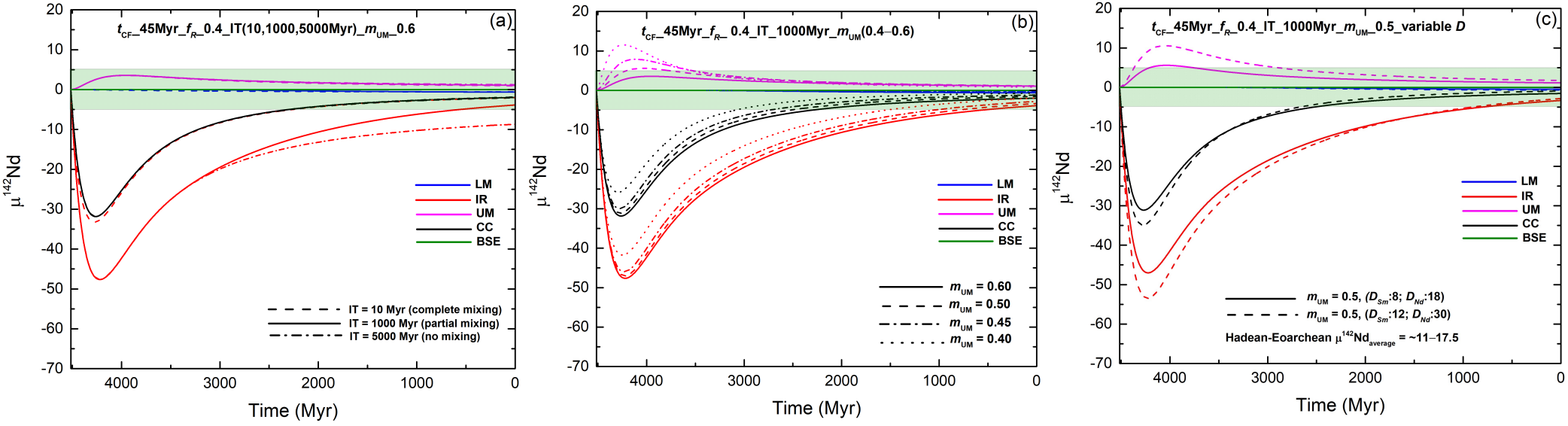
(a)
t_{CF}_45Myr_f_R_0.4_IT(10,1000,5000Myr)_m_{UM}_0.6
LM
IR
UM
CC
BSE
IT = 10 Myr (complete mixing)
IT = 1000 Myr (partial mixing)
IT = 5000 Myr (no mixing)
μ^{142}Nd
Time (Myr)
(b)
t_{CF}_45Myr_f_R_ 0.4_IT_1000Myr_m_{UM}(0.4–0.6)
LM
IR
UM
CC
BSE
m_{UM} = 0.60
m_{UM} = 0.50
m_{UM} = 0.45
m_{UM} = 0.40
μ^{142}Nd
Time (Myr)
(c)
t_{CF}_45Myr_f_R_0.4_IT_1000Myr_m_{UM}_0.5_variable D
LM
IR
UM
CC
BSE
m_{UM} = 0.5, (D_{Sm}:8; D_{Nd}:18)
m_{UM} = 0.5, (D_{Sm}:12; D_{Nd}:30)
Hadean-Eoarchean $\mu^{142}Nd_{average}$ = ~11–17.5
μ^{142}Nd
Time (Myr)

Figure 11

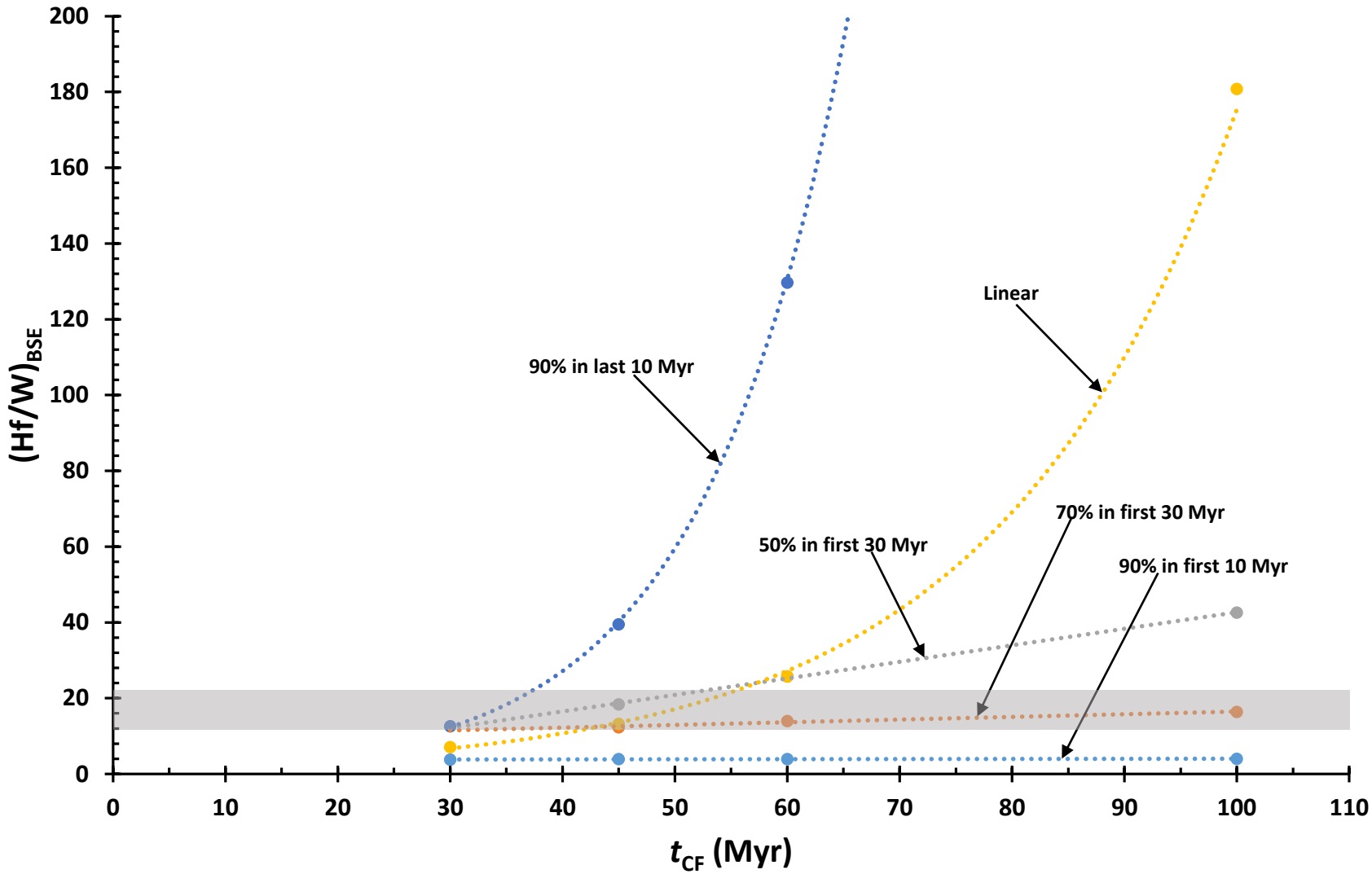
200
180
160
140
120
100
80
60
40
20
0
(Hf/W)BSE
0
10
20
30
40
50
60
70
80
90
100
110
tCF (Myr)
90% in last 10 Myr
Linear
70% in first 30 Myr
50% in first 30 Myr
90% in first 10 Myr

Figure 12

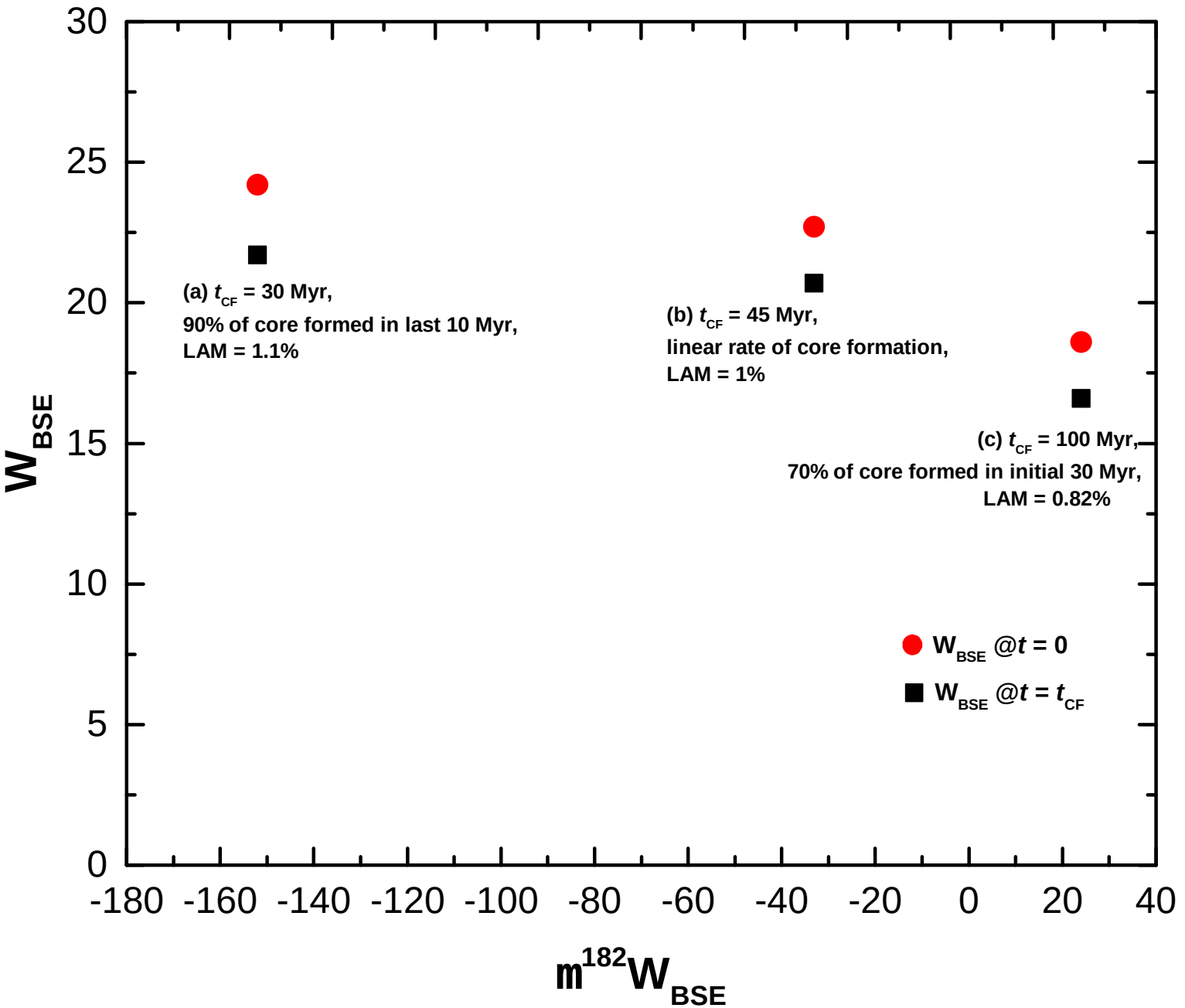
30
25
20
15
10
5
0
-180
-160
-140
-120
-100
-80
-60
-40
-20
0
20
40
W_{BSE}
$m^{182}W_{BSE}$
(a) t_{CF} = 30 Myr,
90% of core formed in last 10 Myr,
LAM = 1.1%
(b) t_{CF} = 45 Myr,
linear rate of core formation,
LAM = 1%
(c) t_{CF} = 100 Myr,
70% of core formed in initial 30 Myr,
LAM = 0.82%
W_{BSE} @t = 0
W_{BSE} @t = t_{CF}

Figure 13

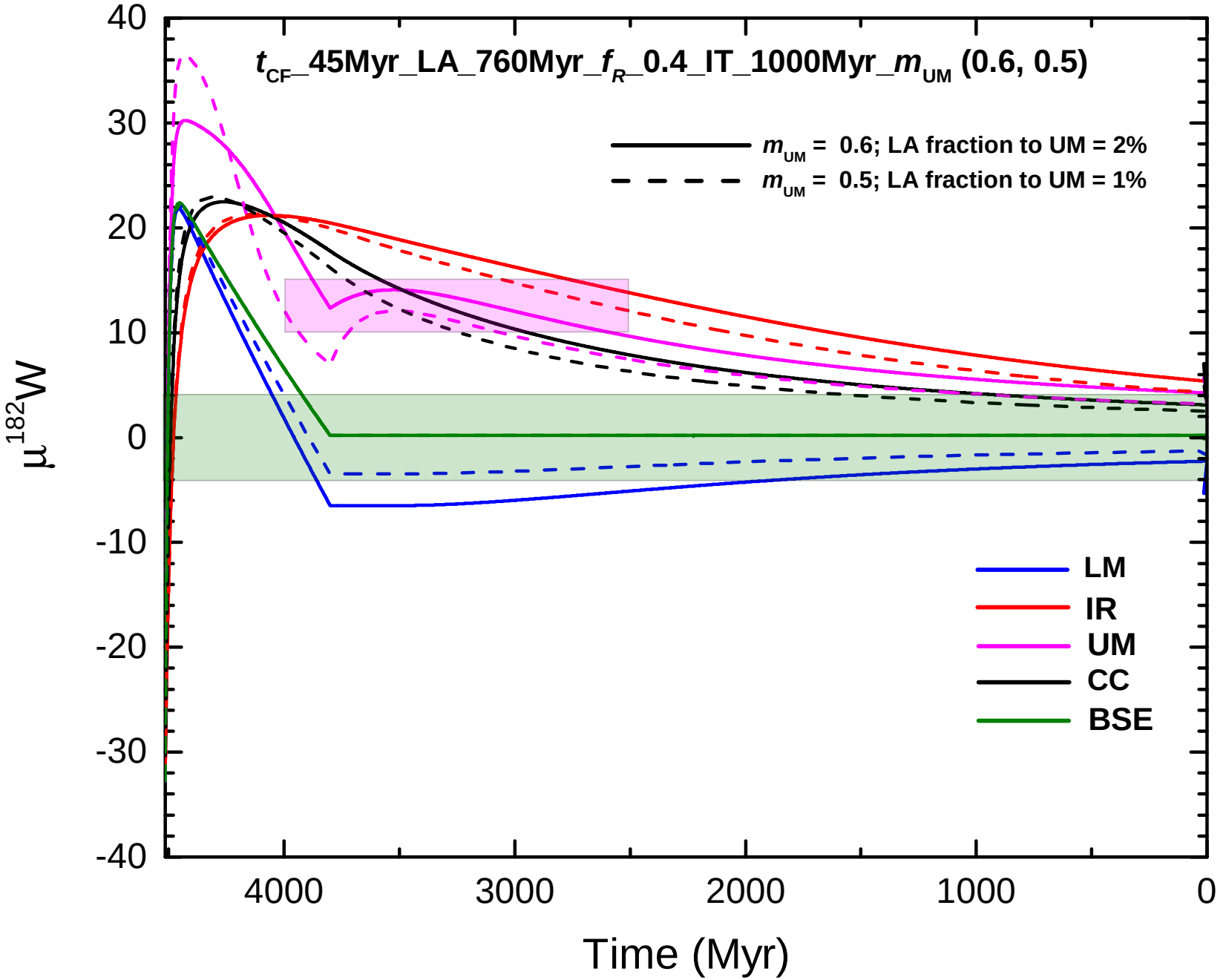
t_{CF}_45Myr_LA_760Myr_f_R_0.4_IT_1000Myr_m_{UM} (0.6, 0.5)
m_{UM} = 0.6; LA fraction to UM = 2%
m_{UM} = 0.5; LA fraction to UM = 1%
LM
IR
UM
CC
BSE
μ^{182}W
Time (Myr)
40
30
20
10
0
-10
-20
-30
-40
4000
3000
2000
1000
0